

1 **Laboratory and numerical investigation of saline intrusion in fractured coastal**  
2 **aquifers**

3 **Georgios Etsias<sup>a,\*</sup>, Gerard A. Hamill<sup>a</sup>, Daniel Campbell<sup>a</sup>, Ryan Straney<sup>a</sup>, Eric M. Benner<sup>a</sup>, Jesus F.**  
4 **Águila<sup>a</sup>, Mark C. McDonnell<sup>a</sup>, Ashraf A. Ahmed<sup>b</sup>, and Raymond Flynn<sup>a</sup>**

5 <sup>a</sup> School of Natural and Built Environment, Queen's University Belfast, Belfast, U.K.

6 <sup>b</sup> College of Engineering, Design and Physical Sciences, Brunel University, London, U.K.

7 Corresponding author: Georgios Etsias ([G.Etsias@qub.ac.uk](mailto:G.Etsias@qub.ac.uk))

8 **Abstract**

9 Laboratory scale experiments and numerical modelling were employed in this study to investigate  
10 saltwater intrusion in fractured aquifers. Saline intrusion was initiated in one homogeneous and six  
11 fractured experimental aquifers containing individual discontinuities of varying length and  
12 orientation. Automated image processing enabled high precision quantification of three intrusion  
13 variables, the toe length of the saline wedge, the width of the mixing zone and the aquifer fraction  
14 occupied by saltwater. A dual porosity model was successfully utilized to recreate the experimental  
15 data and expand the study's findings through rigorous sensitivity analysis. The presence of fractures  
16 significantly impacted all three intrusion variables under consideration. The length of intrusion was  
17 negatively correlated to the horizontal fracture's distance from the systems' seaward boundary. It was  
18 demonstrated that for the same fractured aquifer, the presence of a discontinuity can either limit or  
19 augment saline intrusion, depending on the applied hydraulic gradient. For gradients steeper than a  
20 critical head difference, at which the toe length was the same for both the fractured and the  
21 equivalent homogeneous aquifer, intrusion was suppressed further seaward, while for milder ones it  
22 intensified. The distance of horizontal fracture from the aquifer's base determined the extend of  
23 intrusion in the vertical direction. In general, the longer the discontinuities were, the more significant  
24 their impact on groundwater dynamics. In the case of vertical fractures, whenever the saline wedges  
25 reached their position, the discontinuities contributed significantly in the widening of the mixing zone,  
26 while having limited effect on the other two intrusion characteristics. In aquifers with discontinuities  
27 adjacent to the aquifers' side boundaries, a distinct distribution of saltwater concentration was  
28 identified, distinguishing them from the rest of the aquifers.

29 **Keywords:**

30 Saline intrusion, Fractures, Sandbox experiments, SUTRA, Dual-porosity model

31

32

33

34

35

36

37

38

## 40 1. Introduction

41 One fourth of the global population depends on freshwater pumped from fractured aquifers (Ford  
42 and Williams, 2007), leading to a significant effort to map them and study their hydrogeological  
43 characteristics (Bakalowicz et al., 2007; Custodio, 2009; Chen et al., 2017; Montiel et al., 2018). The  
44 expected increase in average water consumption, alongside sea level rise due to global warming, is  
45 anticipated to intensify saltwater intrusion (SWI) in coastal aquifers. Since fractured systems are more  
46 vulnerable to saltwater intrusion than other aquifer types (Arthur et al., 2007), understanding the  
47 physical mechanisms governing this phenomenon is of utmost importance. Saline intrusion has been  
48 studied in fractured aquifers on multiple locations worldwide, including Canada (Allen et al., 2003),  
49 France (Arfib and Charlier, 2016), Greece (Arfib and Marsily, 2004), Ireland (Perriquet et al., 2014),  
50 Italy (Masciopinto, 2006), Korea (Lim et al., 2013), the United Kingdom (MacAllister et al., 2018) and  
51 the United States (Xu et al., 2016).

52 Numerical modelling is a long established tool for simulating groundwater flow in real world systems.  
53 The numerical approaches employed in the simulation of fractured porous media can be grouped into  
54 two categories, implicit and explicit fracture representation models (Sebben et al., 2015; Berre et al.,  
55 2018). Implicit fracture representation approaches include single continuum or equivalent porous  
56 medium (EPM) models and dual porosity models (DPM). EPM models (Scalnon et al., 2003; Giudici et  
57 al., 2012) are single continuum models in which the fractures are represented by adapting the  
58 permeability of the porous medium, according to the characteristics of the existing fractures. Dual  
59 porosity models (Larsbo and Jarvis, 2005; Fahs et al., 2014) consist of two continua; the matrix, which  
60 represents the porous medium and the fracture, which usually has much higher porosity and  
61 permeability values. Explicit fracture representation approaches include discrete fracture matrix  
62 (DFM) and discrete fracture network (DFN) models. In DFM models the fluid is located in the explicitly  
63 represented fractures and the surrounding porous medium alike. DFM models preserve some  
64 fractures, while the rest are upscaled and replaced by averaged porous medium quantities. Two  
65 dimensional DFM models incorporate fractures as 2-dimensional elements (Jaffré et al. 2005; Angot  
66 et al. 2009; Flemisch et al. 2017; Koohbor et al. 2020). DFN models explicitly represent the majority of  
67 discontinuities present in a fractured aquifer, and fluid flow occurs mainly within the fracture network.  
68 Two-dimensional DFN models represent the geometrical properties of each individual fracture,  
69 incorporating them, as 1-dimensional line boundaries between elements (Quinn et al., 2006;  
70 Papadopoulou et al., 2008; Hirthe and Graf, 2015; Sebben and Werner, 2016; Ren et al., 2017).  
71 Similarly, in 3-d DFN models, fractures are expressed as 2-dimensional planes. The application of each  
72 method is associated with specific benefits and limitations (Samardzioska and Popov, 2005; Blessent  
73 et al., 2013). EPM approaches are characterized by low levels of computational and model complexity,  
74 coming at the cost of oversimplification, that results in inability to represent groundwater flow  
75 dynamics in more complex problems. Dual porosity models are generally more successful in simulating  
76 the impact of fractures on groundwater flow, to do so though, they introduce different parameters,  
77 such as hydraulic conductivity inside the discontinuities and exchange rate coefficients between the  
78 matrix and fractures, which are difficult to determine accurately. By contrast, DFM and DFN models  
79 are computationally intensive, while the explicit mapping of discontinuities in real-world aquifers is  
80 oftentimes problematic.

81 EPM models are prevalent in regional level studies of SWI in fractured coastal aquifers (Nocchi and  
82 Salleolini, 2013; Romanazzi et al., 2015; De Filippis et al., 2016; Steiakakis et al., 2016; Zhao et al.,  
83 2016). Dual porosity modelling is more commonly utilized to simulate saline intrusion in aquifers with  
84 existing conduit networks, this bigger discontinuity size permits a more precise determination of the

85 network's position inside the aquifers. In the majority of these investigations, flow is considered  
86 Darcian both in the porous medium and in the fractures (Xu et al., 2018; Feo et al., 2019; Kreyns et al.,  
87 2020). Nevertheless, multiple numerical approaches have been proposed to incorporate turbulent  
88 flow inside the conduits (Arfib and Marsily, 2004; Xu and Hu, 2017; Xu et al., 2019;). Sebben et al.  
89 (2015) and Mozafari et al. (2018) simulated a variation of the well-known Henry problem in 2-  
90 dimensional aquifers with well-defined networks of individual fractures using DFN modelling. Koohbor  
91 et al. (2019) quantified the impact that the uncertainty associated with the position and density of  
92 fractures, in discrete fracture networks, has on the simulated saline intrusion dynamics. Both Dokou  
93 and Karantzas (2012) and Khadra and Stuyfzand (2018) created hybrid models combining the EPM and  
94 DFN approaches in order to optimize SWI simulation in karst systems.

95 Experimental sandbox setups have been used successfully over the years to investigate saline  
96 intrusion in homogeneous (Robinson et al., 2016, Li et al., 2018; Takahasi et al., 2018; Armanuos et  
97 al., 2019) and heterogeneous aquifers (Konz et al., 2008; Vithanage et al., 2012; Dose et al, 2013; Liu  
98 et al., 2013; Mehdizadeh et al., 2014;). Multiple studies have indicated the significant impact of  
99 heterogeneity on SWI dynamics (Abdulhalik and Ahmed, 2017a, b; Houben et al., 2017). Nevertheless,  
100 saline intrusion in fractured aquifers has never been studied on a sandbox setup. Laboratory  
101 investigations of solute transport in fractured systems have been conducted by Li (2004) and Faulkner  
102 et al. (2009). In both studies, glass beads were utilized to recreate the porous medium. In the first  
103 investigation, the aquifer had a central vertical conduit running from top to bottom, while in the  
104 second study a single horizontal channel was present at the aquifer's lower boundary.

105 The current study employed sandbox experiments coupled with numerical modelling to study saline  
106 intrusion in fractured coastal systems. To the best of the authors' knowledge, this is the first time that  
107 SWI in fractured aquifers has been methodically investigated on a laboratory scale. Head induced  
108 saline intrusion was initiated across six fractured aquifers, with the experimental data obtained being  
109 benchmarked against measurements done on a homogeneous system. The study quantified the  
110 impact that the position, size and orientation of individual fractures have on the standard saltwater  
111 intrusion characteristics of toe length (TL) of the intruding wedge and the width of the mixing zone  
112 (WMZ). Unlike in previous investigations, these intrusion variables were measured with high accuracy,  
113 utilizing advanced image analysis techniques (Robison et al., 2015; Etsias et al., 2020 a). The laboratory  
114 data were successfully recreated using numerical simulations so that the sandbox measurements were  
115 supplemented by an in-depth sensitivity analysis, further expanding the conclusions derived by the  
116 experimental observations. This study constitutes a contribution towards outlining the basic  
117 mechanisms of SWI in fractured porous media, while its results could assist in the successful  
118 management and protection of real-world coastal fractured aquifers.

## 119 **2. Experimental setup**

120 The sandbox apparatus depicted in Figure 1a was employed in deriving the experimental data of this  
121 study. It comprised two cylindrical tanks and a thin central viewing chamber of dimensions 0.38 m ×  
122 0.15 m × 0.01 m. Red food colouring (E129 Allura Red AC Granular) was mixed with saltwater at a  
123 concentration of 0.15 g/L. The density of the dyed saltwater was equal to 1025 kg/m<sup>3</sup>. Transparent  
124 glass beads with a diameter of 1090 μm, supplied by Whitehouse Scientific®, were siphoned into the  
125 viewing chamber to recreate the porous medium of the aquifer. Freshwater was constantly introduced  
126 at the bottom of the left chamber, while the right cylinder was filled with dyed saltwater. The water  
127 level at each side of the chamber was regulated using two adjustable height outflow outlets (Figure  
128 1b), placed at the top of the side tanks, while it was constantly monitored by two ultrasonic sensors  
129 (Figure 1c) with an accuracy of 0.2 mm. Two laser-cut mesh screens were utilized to secure the glass  
130 beads inside the central chamber. Experimental investigations were performed in a dark room; the

131 necessary illumination was provided by two Camtree® 600 LED panels. A Nikon D850 Digital SLR  
132 Camera recorded the experimental images at five-minute intervals. The laboratory apparatus was  
133 presented in detail by Robinson et al. (2015).

134 (Position of Figure 1)

135 Stainless steel mesh screens with 1 mm openings were used to recreate the aquifer fractures. The  
136 mesh was manually moulded around a steel rod with an 8 mm diameter. Three hollow mesh cylinders  
137 with lengths of 35 cm, 15 cm and 10 cm were created (Figure 2). These structures were placed at pre-  
138 determined positions inside the sandbox's viewing chamber, recreating six unique laboratory  
139 fractured aquifers (Figure 3). In four cases, the fractures were horizontally oriented, while in the  
140 remaining two they were vertical in orientation. In the horizontally fractured aquifers, the cylindrical  
141 mesh was placed at the middle of the viewing chamber's height. The first aquifer included the longer  
142 fracture (35 cm), crossing most of the porous medium, while in the remaining three test configurations  
143 the 15 cm long cylinder was located centrally on the test area mid-point and at the left and right  
144 aquifer boundaries respectively. In the vertically fractured test cases, the 10 cm long fracture was  
145 placed at the test mid-point and at a distance of 10 cm from the right boundary of the aquifer. In the  
146 interests of clarity, the laboratory aquifers will henceforth be referred to according to their  
147 corresponding fracture position: horizontal-long (Figure 3b), horizontal-middle (Figure 3c), horizontal-  
148 left (Figure 3d), horizontal-right (Figure 3e), vertical-middle (Figure 3f) and vertical-right (Figure 3g).  
149 Testing was also conducted on a homogeneous aquifer, without any fractures, that served as a  
150 benchmark case for this investigation (Figure 3a).

151 (Position of Figure 2)

152 This is the first ever laboratory study of saltwater intrusion in fractured aquifers. In the absence of any  
153 similar investigations, sandbox studies of SWI, alongside fieldwork investigations of saline intrusion in  
154 real world fractured hydrological systems, were employed to validate the suitability of the  
155 experimental setup in the approximation of fractured aquifers. Glass beads of comparable size have  
156 been utilized in multiple laboratory studies of saline intrusion. Zhang et al. (2001 and 2002) used glass  
157 beads with a diameter of 725  $\mu\text{m}$ , Goswami and Clement (2007) and Chang and Clement (2013)  
158 employed 1.1 mm wide glass spheres, while Konz et al. (2009) studied SWI in heterogeneous aquifers  
159 using glass beads of sizes varying between 0.6 mm and 2.2 mm. An intrinsic flow test on the  
160 experimental domain allowed calculation of the permeability of the porous media using Darcy's law.  
161 Permeability and porosity were equal to  $1.83 \times 10^{-9} \text{ m}^2$  and 0.385, respectively. These results agreed  
162 with the values reported by Robinson et al. (2015, 2016) for the same laboratory apparatus. Glass  
163 beads of similar size have been utilised by Abdelgawad et al. (2017) and Abdoulhalik and Ahmed  
164 (2017a,b) in experimental investigations of saltwater upconing.

165 The permeability measured in the laboratory porous medium was compared with values of  
166 permeability in real world fractured aquifers. De Fillipis et al. (2016) presented a study of saline  
167 intrusion in a karstic coastal aquifer in the Taranto area of Northern Italy. The lowest permeability  
168 values (of the order of  $10^{-4} \text{ m/s}$ ) were calculated inland and along the extremely western coast, while  
169 the central and eastern coastline part of the aquifer had a hydraulic conductivity of 0.1 m/sec, or  
170 approximately  $9.07 \times 10^{-9} \text{ m}^2$ . In an investigation of SWI in a fractured aquifer in Crete, Greece  
171 (Steiakakis et al., 2016) a permeability of  $1.35 \times 10^{-10} \text{ m}^2$  was reported for the limestone portion of the  
172 hydrological system. A comparable permeability value was identified for the fracture-karst aquifer in  
173 Zhoushuizi district of Dalian City in northern China (Zhao et al., 2016). Xu and Hu (2017) introduced a  
174 numerical model for simulating seawater intrusion to a coastal karst aquifer with a conduit system. A  
175 porous medium permeability equal to  $2.4 \times 10^{-9} \text{ m}^2$  was derived from previous field scale studies

176 (Loper et al., 2005; Kincaid and Werner, 2008; Xu et al., 2016) of the Floridan aquifer in the Woodville  
177 Karst Plain, in Florida (USA). Finally, a study of the coastal carbonate aquifer in western Cuba  
178 (Hernandez and Diaz, 2019) reported an aquifer permeability equal to  $1.1 \times 10^{-9} \text{ m}^2$ . The real-world  
179 fractured aquifer permeabilities values presented in this paragraph, have a difference of less than an  
180 order of magnitude from the permeability of the utilised glass bead medium. This validates the current  
181 laboratory setup as an acceptable approximation of saltwater dynamics in fractured hydrological  
182 systems.

183 The sandbox fracture permeability was determined via sensitivity analysis, conducted using the  
184 numerical model presented in the next session. The fractures (steel mesh tube) were approximately  
185 100 times more permeable than the surrounding porous medium (glass beads). This permeability ratio  
186 is in agreement with fieldwork investigations of fractured aquifers. McAllister et al. (2018) in their  
187 study of the Seaford and Lewes Nodular Chalk formations in the UK, reported intrinsic fracture  
188 permeabilities 100 to 150 times larger than the rest of the aquifer. Similarly, Xu and Hu (2017)  
189 identified a conduit network that was 250 times more permeable than the porous medium of the  
190 Floridian karst aquifer.

191 In the initial stage of each experiment, freshwater occupied the whole aquifer. Saltwater was  
192 introduced to the system by applying a hydraulic head difference  $dH = 6 \text{ mm}$  between the two side  
193 chambers of the laboratory apparatus. After the stabilization of the saline wedge, a new phase of  
194 saline intrusion was initiated by modifying the hydraulic head difference from 6mm to 4mm. In the  
195 final part of the experiments saltwater retreat was generated by applying a steeper hydraulic gradient  
196 ( $dH = 4 \text{ mm} - 5 \text{ mm}$ ) in the aquifer. The resulting hydraulic gradients were similar to those documented  
197 for various real world aquifers (Attanayake and Sholley, 2007; Ferguson and Gleesson, 2012). The total  
198 measurement time varied between 160 and 180 minutes in the seven investigated cases, depending  
199 on the time needed for the saline wedge to stabilize after changing the head difference. During the  
200 experiment, water in the right cylinder was monitored using a YSI Professional Plus Instrument (Pro  
201 Plus) water quality meter. The salinity values for all six experiments, obtained at five-minute intervals,  
202 demonstrated minimum variation (Figure S1 of the supplementary material) indicating that water  
203 salinity in the right chamber did not reduce due to the outflow of freshwater through the porous  
204 medium.

205 The automated image analysis algorithms introduced by Robinson et al. (2015) and Etsias et al. (2020  
206 a and b) were utilized to successfully post-process the acquired experimental images. An Artificial  
207 Neural Network (ANN) with a single hidden layer, consisting of 10 neurons, was employed to recreate  
208 saltwater concentration fields from the corresponding Light Intensity (LI) values of the laboratory test  
209 images (Figure 3). Two variables were calculated utilizing image processing to quantify the effect of  
210 fractures on aquifer saline intrusion: TL and WMZ. TL was deemed equivalent to the horizontal  
211 distance between the saltwater boundary of the laboratory aquifer and the point where the 50 %  
212 saltwater concentration isoline intersected with the bottom of the aquifer, while WMZ equated to the  
213 average vertical distance between the 25 % and 75 % saltwater concentration isolines. The automated  
214 calculation of these variables was described in detail by Robinson et al. 2015.

### 215 **3. Numerical modelling**

216 The experimental saltwater flow fields were simulated utilizing a 2-dimensional, saturated-  
217 unsaturated, variable-density groundwater flow model in SUTRA (Voss and Provost, 2010), where the  
218 fractures were modelled discretely as 2-dimensional elements (DFM 2D/2D). Permeability and  
219 porosity were equal to  $1.83 \times 10^{-9} \text{ m}^2$  and 0.385, respectively. Fracture permeability was determined,  
220 via sensitivity analysis, being 100 times larger than that of the matrix, while the porosity of fractures

221 was set equal to 1. Since the size of the mesh tubes was approximately 0.8 cm, and turbulent flow is  
222 not relevant inside fractures with a diameter of less than 1 cm (White et al., 2019), Darcian flow was  
223 considered in both media (matrix and fracture). The x-z two-dimensional flow model, with dimensions  
224 of 0.38 m × 0.134 m, was discretized with a finite element mesh with quadrangular elements of a size  
225 of  $1.22 \times 10^{-3}$  m. The element size complied with the Peclet number criterion (Voss and Souza 1987),  
226 while the applied dispersivity values were within the range introduced by Abarca and Clement (2009).  
227 Unsaturated flow was simulated utilizing the van Genuchten equation (van Genuchten, 1980). Van  
228 Genuchten parameters were determined according to values measured in laboratory testing for glass  
229 beads of comparable size (Benson et al. 2014, Sweijan et al. 2017). A hydrostatic freshwater (C = 0 %)   
230 boundary condition was applied on the left boundary while a hydrostatic saltwater (C = 100 %)   
231 boundary condition was implemented on the right boundary of the aquifer. A necessary step towards  
232 the successful numerical recreation of the laboratory data was the precise identification of the  
233 position of the fracture in each test case. This was achieved through image analysis of the original  
234 experimental figures and the subsequent distribution of all the corresponding elements of the  
235 numerical model in either the matrix or the fracture medium. The simulation time for each test case  
236 was similar to the equivalent experimental duration, while the time-step was equal to 1 sec. Model  
237 parameters are listed in Table 1. A comparison between experimental and numerical results is  
238 presented in Figures 3 and 4.

239 (Position of Table 1)

240 The conclusions about the impact of fractures on SWI, derived from experimental observations, were  
241 investigated further through a rigorous sensitivity analysis using the aforementioned numerical  
242 model. In total four different model setups were created, in three of them the fractures' orientation  
243 was horizontal while in the fourth one it was vertical. This sensitivity analysis expanded the study's  
244 findings on the effect of the fractures' position, orientation and length on aquifer saltwater dynamics.

## 245 **4. Results and discussion**

### 246 **4.1 Experimental results**

247 The experimental saltwater flow fields that were generated inside the sandbox setup, by a hydraulic  
248 head difference between the left and right aquifer boundaries equal to  $dH = 4\text{mm}$ , are presented in  
249 Figure 3. The saline concentration fields derived by experimental image analysis and numerical  
250 modelling (SUTRA) are displayed alongside them. Alongside saltwater concentration, SUTRA calculates  
251 the flow velocity vectors at each individual element. The flow streamlines plotted on top of the  
252 numerical saltwater concentration fields in the third column of Figure 3 were generated by feeding  
253 the numerical flow velocities into the streamslice.m built-in MATLAB equation. The results  
254 demonstrated that the position, size and orientation of discontinuities have a significant impact on  
255 the extent of saltwater intrusion, as well as the shape of saline wedges in fractured systems. The toe  
256 length has been a long established metric of the extend of saline intrusion. Nevertheless, in cases like  
257 the horizontal-long aquifer (Figure 3b), even though the observed TL value was relatively big, the  
258 actual volume of the aquifer occupied by saltwater was disproportionally small. On that account, the  
259 uniquely shaped freshwater - saltwater interfaces, generated by the presence of high permeability  
260 fractures, required the use of a supplementary variable to help quantify and assess the successful  
261 study of SWI. This novel variable, now termed as the saline volume fraction, corresponded to the  
262 fraction of the porous medium in which saltwater concentration was higher than 90%. It was  
263 calculated with high accuracy by the aforementioned image analysis algorithms and has been utilized  
264 for the first time in this study.

265

(Position of Figure 3)

266 The numerical model successfully recreated the laboratory results for all three distinct intrusion and  
267 retreat ( $dH = 6 \text{ mm} - 4 \text{ mm} - 5 \text{ mm}$ ) experimental phases, for all the tested cases (Figure 4). In all  
268 cases, there is excellent temporal agreement between the measured values of TL and those obtained  
269 from the numerical simulations. Furthermore, it proved that using a dual-porosity model to simulate  
270 the sandbox data was a valid choice, and that this model can be safely employed to both interpret the  
271 physical mechanisms affecting SWI in the specific laboratory aquifers, as well as to further expand any  
272 conclusions derived from their study. As expected, the experimental TL was negatively correlated with  
273 the applied hydraulic gradient. The difference between the three steady state TL values (Table 2) was  
274 more significant in the horizontal-long aquifer, where  $\Delta TL_{6-4\text{mm}} = +25.95 \text{ cm}$  and  $\Delta TL_{4-5\text{mm}} = -11.83 \text{ cm}$ ,  
275 while it was minimum for the horizontal-right case,  $\Delta TL_{6-4\text{mm}} = +8.7 \text{ cm}$  and  $\Delta TL_{4-5\text{mm}} = -5.78 \text{ cm}$ . This  
276 demonstrated that, the size and position of the discontinuity can significantly affect the impact of  
277 hydraulic head difference on the extend of saline intrusion. Every change in the hydraulic gradient was  
278 followed by an initial, rapid adjustment of the toe length, which subsequently stabilized. The time to  
279 reach steady state in each intrusion and retreat phase did not vary much between the six investigated  
280 fractured cases. This is in agreement with the laboratory findings of Robinson et al. (2016) indicating  
281 that this time depends solely on the permeability of the porous medium, which was the same in all  
282 laboratory setups.

283

(Position of Figure 4)

284

(Position of Table 2)

285 The three variables outlining the effect of fractures on saline intrusion: TL, WMZ and the percentage  
286 of aquifer saline volume, were quantified. Their values were benchmarked against the SWI  
287 characteristics in the homogeneous laboratory aquifer with the same permeability and porosity values  
288 (Table 3). It was established that, in comparison to the homogeneous case, TL was significantly longer  
289 for the horizontal-long and horizontal-middle aquifers, by 13.8 % and 18.7 % respectively, while it was  
290 about 19.9 % and 6.9 % shorter for the horizontal-left and horizontal-right cases. No quantifiable  
291 deviation in the TL values was observed for the systems with vertical fracture orientation. The mixing  
292 zone in all the fractured cases was wider than that in the homogeneous aquifer. In particular, for the  
293 horizontal-long, horizontal-middle and vertical-right systems, WMZ was more than double the width  
294 of the benchmark case (220 % ~ 285 % of the homogeneous WMZ), while for the remaining three  
295 fractured aquifers it was between 21 % and 52 % wider. The total volume fraction of the aquifer  
296 occupied by the saline wedge was significantly smaller for the horizontal-long and horizontal-left  
297 cases, being equal to just 49.1 % and 78.2 % of the equivalent saline volume fraction in the  
298 homogeneous case. In the remaining fractured aquifers saline volume fraction did not deviate  
299 significantly, ranging between 93.5 % and 105.9 % of the benchmark case.

300

(Position of Table 3)

301 To assess the interpretation of the acquired experimental data and to outline the basic physical  
302 mechanisms behind the impact of fractures on SWI dynamics, the velocity vector fields of the seven  
303 investigated hydraulic systems were recreated using SUTRA (Figure 5). In Figure 5, the magnitude of  
304 flow velocities is expressed with varying colour instead of varying vector lengths, as it is commonly  
305 demonstrated (e.g. Abdoulhalik and Ahmed 2017a). This was deliberately chosen by the authors to  
306 assess velocity visualization, since freshwater, both inside the fractures and the porous medium, flows  
307 with a velocity that is at least an order of magnitude greater than that of the saltwater. Figure 5a  
308 depicts the typical flow velocity distribution occurring during SWI on a homogeneous aquifer. This

309 constitutes a well-documented mechanism, the less dense freshwater overtops saltwater and  
310 outflows from the upper right area of the quasi 2-dimensional system. Flow velocity is considerably  
311 higher for the freshwater than the saltwater and its magnitude peaks around the outflow zone. In the  
312 simulated aquifer depicted in Figure 5b (horizontal-long), two distinct zones of higher velocity were  
313 observed at the entrance and exit of the long fracture. The presence of the fracture caused the  
314 majority of freshwater mass transport to occur through it, while at the same time limiting the flow of  
315 freshwater in the rest of the system, as depicted by the smaller velocity (dark blue) vectors around  
316 the central mesh cylinder. This absence of freshwater at the lower part of the aquifer resulted in longer  
317 saline intrusion near the aquifer's bottom. Saltwater did not intrude over the fracture, accounting for  
318 the relatively small portion of the aquifer being occupied by the saline wedge (Table 3). The horizontal  
319 - middle aquifer (Figure 5c) constituted a hydraulic system similar to the horizontal – long one, with  
320 the exception of a shorter fracture. Yet again, two distinct zones of higher freshwater velocity were  
321 documented at the fracture's edges. The upward movement of freshwater towards the fracture once  
322 more augmented SWI. Freshwater outflow from the fracture's right edge contributed to the saline  
323 wedge's distinct shape. Lu et al. (2013) indicated that according to conservation of mass, separation  
324 of flow streamlines along the freshwater - saltwater interface results in the widening of the mixing  
325 zone. This separation, observed in the areas directly underneath the horizontal discontinuities (Figures  
326 3b and 3c), alongside the small difference between the flow velocities of the two liquids at the same  
327 zone, attributed for the distinctively wider mixing zone in these two systems. The saline volume  
328 fraction of the horizontal - middle system was equal to 105.9 % of the saline volume in the benchmark  
329 homogeneous case.

330

(Position of Figure 5)

331 In the horizontal-left (Figure 5d) and horizontal-right (Figure 5e) laboratory aquifers the same fracture  
332 was placed at diametrically opposite positions, resulting in two distinct saltwater concentration  
333 distributions. In the horizontal-left system the majority of freshwater inflow into the porous medium  
334 occurred through the fracture. Two distinct velocity zones were observed in the aquifer: a low velocity  
335 one directly above and below the fracture, and a relatively large area of high velocity vector fields at  
336 the fracture's right edge. The presence of faster moving freshwater at the centre of the system  
337 resulted in the seaward suppression of saltwater, while the saline wedge's shape was comparable to  
338 that of the homogeneous case albeit with a smaller TL (Table 2). In the horizontal-right aquifer, where  
339 the fracture was in direct proximity with the saltwater boundary, the majority of the water outflow  
340 from this discontinuity as depicted by the relatively lower velocities at the upper right edge of the  
341 system. These two zones of water outflow caused by the position of the cylindrical mesh resulted in a  
342 uniquely shaped saltwater wedge. Yet again, the wider mixing zone directly above the fracture should  
343 be attributed to the separation of streamlines. The total saline volume in this system was equivalent  
344 to 93.5 % of the saltwater volume in the homogeneous case.

345 In the experimental aquifers with vertically oriented fractures, the observed steady-state saltwater  
346 wedges were similar in shape and size to the one recreated in the homogeneous aquifer. In particular,  
347 for the vertical-middle and vertical-right systems, TL equalled to 97.2 % and 99.5 % of the benchmark  
348 case, while saline volume corresponded to 97.9 % and 100.9 % of the saltwater in the homogeneous  
349 aquifer. The vector fields presented in Figures 5f and 5g indicate that the impact of these fractures on  
350 the total distribution of flow was limited. In the vertical-middle case, where the saline wedge never  
351 reached the hollow mesh cylinder, the fracture caused a slight variation in the direction and  
352 magnitude of the velocities in its interior that had limited effect on the rest of the system. On the  
353 other hand, in the vertical-right aquifer where the saltwater wedge extended beyond the fracture's  
354 position, the velocity vector fields inside the mesh structure indicate the intensification of the water



355 recirculation that normally occurs inside the saline wedges. This increased water recirculation justifies  
356 the widening of the mixing zone around the fracture, documented in both Figures 3g and Table 3.  
357 Although this phenomenon was previously reported in purely numerical investigations (Sebben et al.,  
358 2015), it was identified on a laboratory scale for the first time in this study.

359 Overall, the experimental data derived from the six fractured aquifers allowed identification of some  
360 preliminary trends concerning the impact that individual fractures have on SWI characteristics. It was  
361 established that depending on its length and position, horizontally oriented fractures can either  
362 augment or suppress saltwater intrusion, while significantly affecting WMZ and the total volume of  
363 intruding saltwater. On the other hand, vertical fractures contributed to the widening of the mixing  
364 zone, but had a limited impact on the actual length and shape of the intruding wedge. These findings  
365 were further expanded in the following section, using a series of sensitivity analysis scenarios.

## 366 **4.2 Sensitivity analysis**

367 The sensitivity analysis presented here comprises four distinct scenarios, each one examining SWI in  
368 five numerical aquifers. The utilized model parameters were the same as those used in simulating the  
369 experimental saltwater concentration fields (Table 1). Saline intrusion was initiated by applying a  
370 hydraulic head difference of 4 mm, while a total run time of 80 minutes ensured that all systems  
371 reached quasi steady-state. A fifth set of numerical simulations, where different values of hydraulic  
372 gradients were applied to the system, supplemented the findings of the first sensitivity analysis  
373 scenario. Unlike the numerical models presented in the previous section in which the fractures' shape  
374 and position were determined using image analysis, all fissures present in this investigation had an  
375 idealized rectangular shape. In order to assess comparison between experimental data and those  
376 derived from the sensitivity analysis, the saltwater concentration fields presented in this section  
377 include only the part of the aquifer that it is visible in the laboratory sandbox setup. When determining  
378 the depth of discontinuities, the whole height of the numerical aquifer was taken into account, instead  
379 of just the part included in the viewing chamber. As a result, discontinuities in this section was placed  
380 approximately two centimetres higher than the fractures in the laboratory test cases of the previous  
381 section.

### 382 **4.2.1 Horizontal position of horizontally oriented fractures**

383 In the first sensitivity analysis setup, the impact of position ( $x$ ) of horizontal fractures on SWI dynamics  
384 was investigated. To do so, five aquifers containing a single horizontal fracture with dimensions of  
385 15.4 cm  $\times$  0.85 cm (126  $\times$  7 elements) were generated. The fractures were placed at the middle of the  
386 aquifers' depth. On the horizontal direction, they were either placed adjacent to the system's vertical  
387 boundaries (Figures 6a.i and 6a.v), at a distance of 5 cm from them (Figures 6a.ii and 6a.iv) or exactly  
388 at the aquifer's centre (Figure 6a.iii). As seen in Figure 6, the closer the fracture was to the freshwater  
389 boundary, the more it contributed to the suppression of saline intrusion, while the closer its proximity  
390 to the seaward edge, the longer the length of the intruding wedge was (Figure 6b). This is in agreement  
391 with the experimental observations presented in section 4.1. The positive correlation between TL and  
392 fracture position ( $x$ ) was disrupted in the case where the fracture was in contact to the sea (right  
393 boundary). The adjacency of the high permeability fracture with the saline boundary created two  
394 zones of water outflow from the porous medium, significantly altering the underlying flow and mass  
395 transport mechanisms. Moreover, the slightly smaller fracture depth in the numerical aquifers of this  
396 section is responsible for the difference between the saltwater concentration field depicted in Figure  
397 6a.v and that in Figure 3e. Similarly, the mixing zone is widened when the velocity difference between  
398 the two fluids is smaller (Figure 6c). This occurred in the low velocity zones underlying the fractures  
399 (Figure 6a). The impact of these zones was greater with increasing proximity to the freshwater –

400 saltwater interface. This resulted in a mixing zone, that was three times wider in the aquifer depicted  
401 in Figure 6a.iv than in the system illustrated in Figure 6a.i. Finally, a positive correlation was  
402 established between the fracture's proximity with the sea boundary and the total volume of the  
403 intruding saltwater (Figure 6d), leading to a maximum difference of up to 13 % between the saline  
404 volume fraction values of the five test cases.

405 (Position of Figure 6)

406 In order to identify the main factors determining whether the presence of a discontinuity results in  
407 less or more extended saline intrusion, a supplemental set of numerical simulations were conducted.  
408 In total four aquifers were investigated: the centrally fractured case, presented in Figure 6a.iii; two  
409 fractured aquifers, with a discontinuity at 7.5 cm from the aquifer's left and right boundary; and a  
410 homogeneous system with similar porous medium characteristics. SWI was initiated in these aquifers  
411 by applying seven distinct values of hydraulic head difference ( $dH = 4 \text{ mm}, 4.5 \text{ mm}, 5 \text{ mm}, 5.5 \text{ mm}, 6$   
412  $\text{mm}, 6.5 \text{ mm}$  and  $7 \text{ mm}$ ). The generated steady-state TL values are presented in Figure 7. The  
413 numerical results indicated that, depending on the applied hydraulic gradient, the same fracture can  
414 lead to an intruding wedge that is either longer or shorter than the one in the equivalent  
415 homogeneous case. The critical head difference, at which TL was the same for both the fractured and  
416 the homogeneous aquifer, was different for each case. Its value was equal to  $dH = 4.17 \text{ mm}$ ,  $dH = 5.97$   
417  $\text{mm}$  and  $dH = 4.88 \text{ mm}$  for the systems fractured on their left side, right side, and in the middle  
418 respectively. The equivalent TL values for these hydraulic gradients were equal to 22.3 cm, 12 cm and  
419 17.1 cm. When compared to the horizontal position (fracture's centre from the seaward boundary) of  
420 the discontinuity in each system,  $x_{\text{left}} = 23.1 \text{ m}$ ,  $x_{\text{right}} = 13.1 \text{ m}$  and  $x_{\text{middle}} = 18.1 \text{ m}$ , a clear linear  
421 relationship between the critical TL value and the discontinuity's position arises. Summarising, the  
422 findings of the numerical investigation proved that the impact of horizontal fractures on the extent of  
423 intrusion depends on both their position and the applied hydraulic gradient. In cases where the  
424 fracture's distance from the seaward boundary was greater than the saline toe length in the equivalent  
425 homogeneous system, for the same hydraulic gradient, the presence of the discontinuity limited the  
426 extent of intrusion, while in cases where this distance was smaller it augmented it. This conclusion has  
427 potentially significant implications for the effective management of real-world fractured aquifers,  
428 since the projected sea-level rise could alter their hydraulic gradient beyond its critical value, thus  
429 leading to a significant and unexpected increase in the extent of saltwater intrusion.

430 (Position of Figure 7)

#### 431 **4.2.2 Depth location of horizontally oriented fractures**

432 Five numerical fractured aquifers were utilized to quantify the effect that the depth below the surface  
433 ( $z$ ) of horizontal discontinuities has on saltwater intrusion. A fracture with the same dimensions to  
434 those described in the previous section was located at a depth from the system's surface equal to  $1/6$ ,  
435  $1/3$ ,  $1/2$ ,  $2/3$  and  $5/6$  of the total aquifer width. As seen in Figure 8, the impact of fractures on the  
436 saltwater – freshwater interface became greater the closer the discontinuity was to the impermeable  
437 lower boundary. For the majority of the test cases, the TL was positively correlated to the fracture's  
438 distance from the aquifer's free surface (Figure 8b). Nevertheless, TL variation between the different  
439 aquifers of this setup was much more limited. The shortest TL (Figure 8a.i) equalled to 94.2 % of the  
440 longest TL case (Figure 8a.v), translating into a difference of less than 2 cm. In comparison, maximum  
441 toe length difference in the previous sensitivity analysis scenario was approximately 11 cm, or a  
442 minimum TL value corresponding to just 58.9 % of the maximum TL. Similar to the previous set of  
443 numerical investigations, this trend did not apply to the last test aquifer (Figure 8a.v), where the length  
444 of the intruding wedge was shorter than the previous cases. The physical mechanism described for

445 the experimental horizontal – middle aquifer (section 4.1) also applied to these numerical aquifers as  
446 well. However, the fracture’s impact proved greater with decreasing distance from the interface of  
447 the two liquids. The correlation between fracture depth (z) and WMZ was similar to that reported for  
448 the toe length (Figure 8c), while the total volume of intruding saltwater was negatively correlated to  
449 the fracture’s distance from the system’s upper boundary (Figure 8d) resulting in an absolute  
450 difference of up to 5 % between the investigated aquifers. For all the scenario’s test cases, saline  
451 volume constituted a fraction (72.3 % - 97.3 %) of the volume in the equivalent homogeneous case.  
452 The current analysis demonstrated that even though the vertical position of a discontinuity has a  
453 limited effect on the final length of the intruding wedge, it can significantly influence the extent of  
454 intrusion at the upper parts of an aquifer. This could constitute a significant finding in the successful  
455 management of real-life fractured systems, where SWI in the upper aquifer region could significantly  
456 damage human activities such as farming (Alam et al., 2017).

457 (Position of Figure 8)

#### 458 **4.2.3 Length of horizontally oriented fractures**

459 The effect of fracture length on saline intrusion dynamics was studied on the third sensitivity analysis  
460 setup. Aquifers with a single horizontal fracture of a width of 0.85 cm and a varying length equal to  
461 1/6, 1/3, 1/2 and 2/3 of the total aquifer length, as well as an aquifer with a fracture spanning from  
462 one aquifer edge to the other, were tested. With the exception of the last case, the numerical results  
463 indicated a positive relationship between fracture length and length of intrusion (Figure 9b). The  
464 longer the discontinuities, the larger the zones of lower freshwater velocity underneath them, leading  
465 to more space occupied by saltwater. The maximum difference between the TL values generated in  
466 this scenario was less than 5 cm. Both WMZ (Figure 9c) and the total volume of the saline water (Figure  
467 9d) were affected by the fracture length in a similar way. The unique shape of the intruding wedge in  
468 the last investigated aquifer (Figure 9a.v), comparable to the interface shape of the horizontal-long  
469 (Figure 3b) experimental system, indicated a fundamentally different flow mechanism. This could be  
470 attributed to the fact that the bulk of the mass transport inside the system occurred exclusively  
471 through its discontinuity, contributing to the limited impact of dispersion effects.

472 (Position of Figure 9)

#### 473 **4.2.4 Horizontal position of vertically oriented fractures**

474 The final sensitivity analysis setup investigated the influence that the position (x) of vertical  
475 discontinuities has on aquifer saline intrusion. Five numerical aquifers with fractures of dimensions  
476 0.85 cm × 11.8 cm placed at different distances from the system’s side boundaries were the basis of  
477 this study (Figure 10a). It was shown that the impact of the discontinuities’ position on the steady-  
478 state length of intrusion was relatively limited, causing a TL variation of less than 12 % between the  
479 five tested cases (Figure 10b). On the other hand, the width of the mixing zone was significantly  
480 affected by the fractures’ location. In aquifers where the intruding saline wedge incorporated the  
481 discontinuities, WMZ widened by up to 12 cm in comparison to the cases where the fractures were  
482 fully covered by freshwater (Figure 10c). This constituted an increase of approximately 400 %. The  
483 correlation between the position of vertical discontinuities and the width of mixing zone is in  
484 agreement with the relationship derived by the experimental measurements (section 4.1) as well as  
485 the numerical findings of Sebben et al. (2015). The impact of flow recirculation effects inside the  
486 discontinuity was more severe on its downstream than its upstream area, i.e. right of the fracture in  
487 the investigated numerical setup. This justifies why the increase in WMZ was larger in the numerical  
488 aquifer depicted on Figure 10a.iv, where the fracture was approximately at the middle of the intruding

489 wedge. Finally, since no significant alteration of the traditional wedge shape was observed in any  
490 aquifer, the trend in the total volume of intruding saltwater was comparable to that of the TL values  
491 (Figure 10d). The deviation of saline volume fraction was 5% or less between the investigated  
492 fractured systems.

493 (Position of Figure 10)

494 The sensitivity analysis results presented here further expanded the findings derived in section 4.1.  
495 Horizontally oriented fractures were proven to have a significant impact in both TL, WMZ and the total  
496 volume of intruding saltwater. In cases where horizontal discontinuities were present further toward  
497 the freshwater reservoir, they tended to limit the extent of saline intrusion, while the opposite  
498 occurred as the fractures were closer to the sea. Even though TL values were relatively unaffected by  
499 the depth in which such fractures were located, their vertical position determined the height up to  
500 which saltwater would intrude. To that effect, the fractures acted as high permeability barriers  
501 confining SWI to the lower aquifer levels. This indicated that the impact of horizontal fractures on  
502 saline intrusion dynamics was greater with increasing length. Finally, vertical fractures widened the  
503 freshwater - saltwater mixing zone, with their effect proving greater when positioned in the middle of  
504 the intruding wedges.

## 505 **5. Conclusions**

506 Saltwater intrusion in fractured unconfined coastal aquifers was studied on a laboratory scale for the  
507 first time in the current paper. Saline intrusion was initiated in a thin sandbox setup by applying three  
508 distinct hydraulic gradients. A total of six fractured systems, with discontinuities of different size and  
509 orientation, were tested alongside one homogeneous aquifer with similar porous medium attributes.  
510 Automated image analysis enabled the recreation of saltwater concentration fields as well as the  
511 precise calculation of three SWI characteristics: the length of intruding wedge, the width of the mixing  
512 zone and the aquifer volume fraction occupied by saltwater. The experimental results were  
513 successfully simulated using a dual porosity model in SUTRA. This model was subsequently employed  
514 in conducting a detailed sensitivity analysis to validate and expand the findings derived from the  
515 laboratory data.

516 It was established that the presence of fractures significantly impacts all three saltwater intrusion  
517 variables. The impact of four specific fracture attributes was investigated, the fracture's horizontal  
518 and vertical position, its length and its orientation. The following conclusions can be drawn:

- 519 • In cases where horizontal discontinuities were present closer to the aquifer's saline boundary,  
520 the extent of saltwater intrusion was generally bigger, while in systems where the fractures  
521 were further away from the sea, the saline wedge was reduced. Rigorous sensitivity analysis  
522 revealed that the extent to which a discontinuity affects the toe length of the intruding wedge  
523 depends on two variables: its horizontal position and the hydraulic gradient applied in the  
524 system. A critical hydraulic head difference was identified as the defining factor behind the  
525 discontinuity's impact on saline intrusion for each specific fractured system. For hydraulic  
526 gradients steeper than this head difference, the fracture's presence limits the intrusion, while  
527 for milder gradients it intensifies it.
- 528 • The vertical distance of horizontal fractures from the aquifer's free surface was positively  
529 correlated to the generated saline wedge length and width of mixing zone, while negatively  
530 correlated to the percentage of saltwater volume. Discontinuities acted similar to high  
531 permeability barriers, confining the saline wedge in the aquifer's lower level.

- 532 • The longer the discontinuities were, the more pronounced their effect was on all three  
533 saltwater intrusion characteristics.
- 534 • Vertical fractures had a limited effect on the length of intrusion and the total aquifer fraction  
535 occupied by saltwater. On the other hand, they had a significant impact on the width of the  
536 mixing zone, resulting in its increase by a factor of up to four, under the scenarios investigated.  
537 This effect was more intense in cases where the fractures were located in the middle of the  
538 saline wedges.
- 539 • Whenever the discontinuities were in contact to the aquifer's freshwater or saltwater side  
540 boundaries, the generated concentration fields deviated significantly from the rest of the  
541 cases, indicating a critical alteration of the underlying flow mechanisms.

542 This study outlined the effects of individual fractures on the dynamics of saltwater intrusion in coastal  
543 aquifers. The two-dimensional nature of the laboratory setup, alongside the simplified geometry of  
544 the investigated fractures and the homogeneous nature of the surrounding porous medium, enabled  
545 the identification of the fundamental physical flow mechanisms generated by the presence of high  
546 permeability - high porosity discontinuities without the uncertainty that usually accompanies the  
547 study of SWI on field scale investigations. Even though derived for idealized conditions, the findings  
548 of this study could be of significant importance for the effective management of real-world fractured  
549 aquifers. Moreover, the precise laboratory data presented in this study may be employed to  
550 benchmark numerical models studying saline intrusion in fractured media. Future work could expand  
551 the conclusions of this study by investigating more complex configurations of fractures with varying  
552 size and orientation, as well as different boundary conditions and porous medium characteristics.

### 553 **Acknowledgements**

554 This work was funded by EPSRC Standard Research (Grant No. EP/R019258/1).

### 555 **References**

- 556 Abarca, E., Clement, T.P., 2009. A novel approach for characterizing the mixing zone of a saltwater  
557 wedge. *Geophys. Res. Lett.* 36 (6), L06402.
- 558 Abdelgawad, A. M., Abdoulhalik, A., Ahmed, A. A., Moutari, S., & Hamill, G. (2018). Transient  
559 Investigation of the Critical Abstraction Rates in Coastal Aquifers: Numerical and Experimental  
560 Study. *Water Resources Management*, 32(11), 3563-3577. doi:10.1007/s11269-018-1988-3
- 561 Abdoulhalik, A., & Ahmed, A. A. (2017a). The effectiveness of cutoff walls to control saltwater intrusion  
562 in multi-layered coastal aquifers: Experimental and numerical study. *Journal of Environmental*  
563 *Management*, 199, 62-73. doi: 10.1016/j.jenvman.2017.05.040
- 564 Abdoulhalik, A., & Ahmed, A. A. (2017b). How does layered heterogeneity affect the ability of  
565 subsurface dams to clean up coastal aquifers contaminated with seawater intrusion? *Journal*  
566 *of Hydrology*, 553, 708–721. doi: 10.1016/j.jhydrol.2017.08.044
- 567 Arfib, B., & Charlier, J.-B. (2016). Insights into saline intrusion and freshwater resources in coastal  
568 karstic aquifers using a lumped Rainfall–Discharge–Salinity model (the Port-Miou brackish  
569 spring, SE France). *Journal of Hydrology*, 540, 148–161. doi: 10.1016/j.jhydrol.2016.06.010
- 570 Arfib, B., & Marsily, G. D. (2004). Modeling the salinity of an inland coastal brackish karstic spring with  
571 a conduit-matrix model. *Water Resources Research*, 40(11). doi: 10.1029/2004wr003147
- 572 Alam, M. Z., Carpenter-Boggs, L., Mitra, S., Haque, M. M., Halsey, J., Rokonzaman, M.,  
573 Moniruzzaman, M. (2017). Effect of Salinity Intrusion on Food Crops, Livestock, and Fish

- 574 Species at Kalapara Coastal Belt in Bangladesh. *Journal of Food Quality*, 2017, 1–23. doi:  
575 10.1155/2017/2045157
- 576 Allen, D.M., Liteanu, E., & Mackie, D.C. (2003). Geologic controls on the occurrence of saltwater  
577 intrusion in heterogeneous and fractured island aquifers, southwestern British Columbia,  
578 Canada. *Proceedings of 2nd International Conference on Saltwater Intrusion in Coastal*  
579 *Aquifers – Monitoring, Modeling, and Management, Mérida, México (2003)*
- 580 Angot, P., Boyer, F., & Hubert, F. (2009). Asymptotic and numerical modelling of flows in fractured  
581 porous media. *ESAIM: M2AN*, 43(2), 239-275. doi: 10.1051/m2an/2008052
- 582 Armanuos, A. M., Ibrahim, M. G., Mahmud, W. E., Takemura, J., & Yoshimura, C. (2019). Analysing the  
583 Combined Effect of Barrier Wall and Freshwater Injection Countermeasures on Controlling  
584 Saltwater Intrusion in Unconfined Coastal Aquifer Systems. *Water Resources Management*,  
585 33(4), 1265–1280. doi: 10.1007/s11269-019-2184-9
- 586 Arthur, J. D., Wood, H. A. R., Baker, A. E., Cichon, J. R., & Raines, G. L. (2007). Development and  
587 Implementation of a Bayesian-based Aquifer Vulnerability Assessment in Florida. *Natural*  
588 *Resources Research*, 16(2), 93–107. doi: 10.1007/s11053-007-9038-5
- 589 Attanayake, P., & Sholley, M. (2007). Evaluation of the hydraulic gradient at an island for low-level  
590 nuclear waste disposal. *IAHS publication*, 312, 237.
- 591 Bakalowicz, M., Hakim, M. E., & El-Hajj, A. (2007). Karst groundwater resources in the countries of  
592 eastern Mediterranean: the example of Lebanon. *Environmental Geology*, 54(3), 597–604.  
593 doi: 10.1007/s00254-007-0854-z
- 594 Benson, C. H., Chiang, I., Chalermyanont, T., & Sawangsuriya, A. (2014). Estimating van Genuchten  
595 Parameters  $\alpha$  and  $n$  for Clean Sands from Particle Size Distribution Data. *From Soil Behavior*  
596 *Fundamentals to Innovations in Geotechnical Engineering*. doi: 10.1061/9780784413265.033
- 597 Berre, I., Doster, F., & Keilegavlen, E. (2018). Flow in Fractured Porous Media: A Review of Conceptual  
598 Models and Discretization Approaches. *Transport in Porous Media*, 130(1), 215–236. doi:  
599 10.1007/s11242-018-1171-6
- 600 Blessent, D., Jørgensen, P. R., & Therrien, R. (2013). Comparing Discrete Fracture and Continuum  
601 Models to Predict Contaminant Transport in Fractured Porous Media. *Groundwater*, 52(1),  
602 84–95. doi: 10.1111/gwat.12032
- 603 Chen, Z., Auler, A. S., Bakalowicz, M., Drew, D., Griger, F., Hartmann, J., ... Goldscheider, N. (2017). The  
604 World Karst Aquifer Mapping project: concept, mapping procedure and map of Europe.  
605 *Hydrogeology Journal*, 25(3), 771–785. doi: 10.1007/s10040-016-1519-3
- 606 Custodio, E. (2009). Coastal aquifers of Europe: an overview. *Hydrogeology Journal*, 18(1), 269–280.  
607 doi: 10.1007/s10040-009-0496-1
- 608 Dose, E. J., Stoeckl, L., Houben, G. J., Vacher, H., Vassolo, S., Dietrich, J., & Himmelsbach, T. (2014).  
609 Experiments and modeling of freshwater lenses in layered aquifers: Steady state interface  
610 geometry. *Journal of Hydrology*, 509, 621–630. doi: 10.1016/j.jhydrol.2013.10.010
- 611 Dokou, Z., & Karatzas, G. P. (2012). Saltwater intrusion estimation in a karstified coastal system using  
612 density-dependent modelling and comparison with the sharp-interface approach.  
613 *Hydrological Sciences Journal*, 57(5), 985–999. doi: 10.1080/02626667.2012.690070

- 614 Etsias, G., Hamill, G., Benner, E., Aguila, J.F., McDonnell, M., Flynn & R., Ahmed, A.A. (2020 a)  
615 Optimizing Laboratory Investigations of Saline Intrusion by Incorporating Machine Learning  
616 Techniques. *Water*, in press.
- 617 Etsias, G., Hamill, G., Benner, E., Aguila, J.F., McDonnell, & M., Flynn (2020 b) The effect of colour  
618 Depth and image resolution on laboratory scale study of aquifer saltwater intrusion.  
619 Proceedings of CERAI, 27 - 28 August 2020, Cork, Ireland.
- 620 Fahs, H., Hayek, M., Fahs, M., & Younes, A. (2014). An efficient numerical model for hydrodynamic  
621 parameterization in 2D fractured dual-porosity media. *Advances in Water Resources*, 63, 179–  
622 193. doi: 10.1016/j.advwatres.2013.11.008
- 623 Faulkner, J., Hu, B. X., Kish, S., & Hua, F. (2009). Laboratory analog and numerical study of groundwater  
624 flow and solute transport in a karst aquifer with conduit and matrix domains. *Journal of*  
625 *Contaminant Hydrology*, 110(1-2), 34–44. doi: 10.1016/j.jconhyd.2009.08.004
- 626 Feo, A., Zanini, A., Petrella, E., Hernández-Díaz, R., & Celico, F. (2019). Analysis of the Saltwater Wedge  
627 in a Coastal Karst Aquifer with a Double Conduit Network, Numerical Simulations and  
628 Sensitivity Analysis. *Water*, 11(11), 2311. doi: 10.3390/w11112311
- 629 Ferguson, G., & Gleeson, T. (2012). Vulnerability of coastal aquifers to groundwater use and climate  
630 change. *Nature Climate Change*, 2(5), 342-345.
- 631 Filippis, G. D., Foglia, L., Giudici, M., Mehl, S., Margiotta, S., & Negri, S. L. (2016). Seawater intrusion in  
632 karstic, coastal aquifers: Current challenges and future scenarios in the Taranto area (southern  
633 Italy). *Science of The Total Environment*, 573, 1340–1351. doi:  
634 10.1016/j.scitotenv.2016.07.005
- 635 Flemisch, B., Berre, I., Boon, W., Fumagalli, A., Schwenck, N., Scotti, A., . . . Tatomir, A. (2018).  
636 Benchmarks for single-phase flow in fractured porous media. *Advances in Water Resources*,  
637 111, 239-258. doi: 10.1016/j.advwatres.2017.10.036
- 638 Ford D, Williams P (2007) *Karst hydrogeology and geomorphology*. Wiley, Chichester, UK
- 639 Genuchten, M. T. V. (1980). A Closed-form Equation for Predicting the Hydraulic Conductivity of  
640 Unsaturated Soils. *Soil Science Society of America Journal*, 44(5), 892–898. doi:  
641 10.2136/sssaj1980.03615995004400050002x
- 642 Giudici, M., Margiotta, S., Mazzone, F., Negri, S., & Vassena, C. (2012). Modelling hydrostratigraphy  
643 and groundwater flow of a fractured and karst aquifer in a Mediterranean basin (Salento  
644 peninsula, southeastern Italy). *Environmental Earth Sciences*, 67(7), 1891–1907. doi:  
645 10.1007/s12665-012-1631-1
- 646 Hirthe, E. M., & Graf, T. (2015). Fracture network optimization for simulating 2D variable-density flow  
647 and transport. *Advances in Water Resources*, 83, 364–375. doi:  
648 10.1016/j.advwatres.2015.07.001
- 649 Houben, G. J., Stoeckl, L., Mariner, K. E., & Choudhury, A. S. (2018). The influence of heterogeneity  
650 on coastal groundwater flow - physical and numerical modeling of fringing reefs, dykes and  
651 structured conductivity fields. *Advances in Water Resources*, 113, 155–166. doi:  
652 10.1016/j.advwatres.2017.11.024

- 653 Khadra, W. M., & Stuyfzand, P. J. (2018). Simulation of saltwater intrusion in a poorly karstified coastal  
654 aquifer in Lebanon (Eastern Mediterranean). *Hydrogeology Journal*, 26(6), 1839–1856. doi:  
655 10.1007/s10040-018-1752-z
- 656 Kincaid, T. R., & Werner, C. L. (2008). Conduit Flow Paths and Conduit/Matrix Interactions Defined by  
657 Quantitative Groundwater Tracing in the Floridan Aquifer. In *Sinkholes and the Engineering  
658 and Environmental Impacts of Karst* (2008) (pp. 288-302).
- 659 Konz, M., Ackerer, P., Meier, E., Huggenberger, P., Zechner, E., & Gechter, D. (2008). On the  
660 measurement of solute concentrations in 2-D flow tank experiments. *Hydrology and Earth  
661 System Sciences*, 12(3), 727–738. doi: 10.5194/hess-12-727-2008
- 662 Konz, M., Younes, A., Ackerer, P., Fahs, M., Huggenberger, P., & Zechner, E. (2009). Variable-density  
663 flow in heterogeneous porous media — Laboratory experiments and numerical simulations.  
664 *Journal of Contaminant Hydrology*, 108(3-4), 168-175. doi:10.1016/j.jconhyd.2009.07.005
- 665 Koohbor, B., Fahs, M., Ataie-Ashtiani, B., Belfort, B., Simmons, C. T., & Younes, A. (2019). Uncertainty  
666 analysis for seawater intrusion in fractured coastal aquifers: Effects of fracture location,  
667 aperture, density and hydrodynamic parameters. *Journal of Hydrology*, 571, 159–177. doi:  
668 10.1016/j.jhydrol.2019.01.052
- 669 Koohbor, B., Fahs, M., Hoteit, H., Doummar, J., Younes, A., & Belfort, B. (2020). An advanced discrete  
670 fracture model for variably saturated flow in fractured porous media. *Advances in Water  
671 Resources*, 140, 103602. doi: 10.1016/j.advwatres.2020.103602
- 672 Kreyns, P., Geng, X., & Michael, H. A. (2020). The influence of connected heterogeneity on  
673 groundwater flow and salinity distributions in coastal volcanic aquifers. *Journal of Hydrology*,  
674 586, 124863. doi: 10.1016/j.jhydrol.2020.124863
- 675 Larsbo, M., & Jarvis, N. (2005). Simulating Solute Transport in a Structured Field Soil: Uncertainty in  
676 Parameter Identification and Predictions. *Journal of Environmental Quality*, 34(2), 621–634.  
677 doi: 10.2134/jeq2005.0621
- 678 Li, G., 2004. Laboratory Simulation of Solute Transport and Retention in a Karst Aquifer, Program in  
679 Geophysical Fluid Dynamics, Florida State University.
- 680 Li, F.L., Chen, X.-Q., Liu, C.-H., Lian, Y.-Q., & He, L. (2018). Laboratory tests and numerical simulations  
681 on the impact of subsurface barriers to saltwater intrusion. *Natural Hazards*, 91(3), 1223–  
682 1235. doi: 10.1007/s11069-018-3176-4
- 683 Lim, J.-W., Lee, E., Moon, H. S., & Lee, K.-K. (2013). Integrated investigation of seawater intrusion  
684 around oil storage caverns in a coastal fractured aquifer using hydrogeochemical and isotopic  
685 data. *Journal of Hydrology*, 486, 202–210. doi: 10.1016/j.jhydrol.2013.01.023
- 686 Liu, Y., Mao, X., Chen, J., & Barry, D. A. (2013). Influence of a coarse interlayer on seawater intrusion  
687 and contaminant migration in coastal aquifers. *Hydrological Processes*, 28(20), 5162–5175.  
688 doi: 10.1002/hyp.10002
- 689 Loper, D. E., Werner, C. L., Chicken, E., Davies, G., & Kincaid, T. (2005). Coastal carbonate aquifer  
690 sensitivity to tides. *Eos, Transactions American Geophysical Union*, 86(39), 353.  
691 doi:10.1029/2005eo390001
- 692 Lu, C., Chen, Y., Zhang, C., & Luo, J. (2013). Steady-state freshwater–seawater mixing zone in stratified  
693 coastal aquifers. *Journal of Hydrology*, 505, 24–34. doi: 10.1016/j.jhydrol.2013.09.017



- 694 Macallister, D., Jackson, M. D., Butler, A. P., & Vinogradov, J. (2018). Remote Detection of Saline  
695 Intrusion in a Coastal Aquifer Using Borehole Measurements of Self-Potential. *Water*  
696 *Resources Research*, 54(3), 1669–1687. doi: 10.1002/2017wr021034
- 697 Martin, V., Jaffré, J., Roberts, J.E. (2005). Modeling fractures and barriers as interfaces for flow in  
698 porous media. *SIAM J. Sci. Comput.* 26(5), 1667–1691. doi:10.1137/s1064827503429363
- 699 Masciopinto, C. (2006). Simulation of coastal groundwater remediation: the case of Nardò fractured  
700 aquifer in Southern Italy. *Environmental Modelling & Software*, 21(1), 85–97. doi:  
701 10.1016/j.envsoft.2004.09.028
- 702 Mehdizadeh, S. S., Werner, A. D., Vafaie, F., & Badaruddin, S. (2014). Vertical leakage in sharp-interface  
703 seawater intrusion models of layered coastal aquifers. *Journal of Hydrology*, 519, 1097–1107.  
704 doi: 10.1016/j.jhydrol.2014.08.027
- 705 Montiel, D., Dimova, N., Andreo, B., Prieto, J., Garcia-Orellana, J., & Rodellas, V. (2017). Assessing  
706 Submarine Groundwater Discharge (Sgd) In Highly Heterogeneous Coastal Karst Aquifers:  
707 Challenges and Solutions. doi: 10.1130/abs/2017cd-292389
- 708 Mozafari, B., Fahs, M., Ataie-Ashtiani, B., Simmons, C. T., & Younes R. (2018). On the use of COMSOL  
709 Multiphysics for seawater intrusion in fractured coastal aquifers. *Proceedings of 25th Salt*  
710 *Water Intrusion Meeting*, 17-22 June 2018, Gdansk Poland.
- 711 Nocchi, M., & Salleolini, M. (2013). A 3D density-dependent model for assessment and optimization  
712 of water management policy in a coastal carbonate aquifer exploited for water supply and fish  
713 farming. *Journal of Hydrology*, 492, 200–218. doi: 10.1016/j.jhydrol.2013.03.048
- 714 Papadopoulou, M. P., Varouchakis, E. A., & Karatzas, G. P. (2009). Terrain Discontinuity Effects in the  
715 Regional Flow of a Complex Karstified Aquifer. *Environmental Modeling & Assessment*, 15(5),  
716 319–328. doi: 10.1007/s10666-009-9207-5
- 717 Perriquet, M., Leonardi, V., Henry, T., & Jourde, H. (2014). Saltwater wedge variation in a non-  
718 anthropogenic coastal karst aquifer influenced by a strong tidal range (Burren, Ireland).  
719 *Journal of Hydrology*, 519, 2350–2365. doi: 10.1016/j.jhydrol.2014.10.006
- 720 Quinn, J. J., Tomasko, D., & Kuiper, J. A. (2006). Modeling complex flow in a karst aquifer. *Sedimentary*  
721 *Geology*, 184(3-4), 343–351. doi: 10.1016/j.sedgeo.2005.11.009
- 722 Ren, F., Ma, G., Wang, Y., Li, T., & Zhu, H. (2017). Unified pipe network method for simulation of water  
723 flow in fractured porous rock. *Journal of Hydrology*, 547, 80–96. doi:  
724 10.1016/j.jhydrol.2017.01.044
- 725 Robinson, G., Ahmed, A. A., & Hamill, G. (2016). Experimental saltwater intrusion in coastal aquifers  
726 using automated image analysis: Applications to homogeneous aquifers. *Journal of Hydrology*,  
727 538, 304–313. doi: 10.1016/j.jhydrol.2016.04.017
- 728 Robinson, G., Hamill, G., & Ahmed, A. A. (2015). Automated image analysis for experimental  
729 investigations of salt water intrusion in coastal aquifers. *Journal of Hydrology*, 530, 350–360.  
730 doi: 10.1016/j.jhydrol.2015.09.046
- 731 Romanazzi, A., Gentile, F., & Polemio, M. (2015). Modelling and management of a Mediterranean  
732 karstic coastal aquifer under the effects of seawater intrusion and climate change.  
733 *Environmental Earth Sciences*, 74(1), 115–128. doi: 10.1007/s12665-015-4423-6

- 734 Samardzioska, T., & Popov, V. (2005). Numerical comparison of the equivalent continuum, non-  
735 homogeneous and dual porosity models for flow and transport in fractured porous media.  
736 *Advances in Water Resources*, 28(3), 235–255. doi: 10.1016/j.advwatres.2004.11.002
- 737 Scanlon, B. R., Mace, R. E., Barrett, M. E., & Smith, B. (2003). Can we simulate regional groundwater  
738 flow in a karst system using equivalent porous media models? Case study, Barton Springs  
739 Edwards aquifer, USA. *Journal of Hydrology*, 276(1-4), 137–158. doi: 10.1016/s0022-  
740 1694(03)00064-7
- 741 Sebben, M. L., Werner, A. D., & Graf, T. (2015). Seawater intrusion in fractured coastal aquifers: A  
742 preliminary numerical investigation using a fractured Henry problem. *Advances in Water  
743 Resources*, 85, 93–108. doi: 10.1016/j.advwatres.2015.09.013
- 744 Sebben, M. L., & Werner, A. D. (2016). A modelling investigation of solute transport in permeable  
745 porous media containing a discrete preferential flow feature. *Advances in Water Resources*,  
746 94, 307–317. doi: 10.1016/j.advwatres.2016.05.022
- 747 Steiakakis, E., Vavadakis, D., Kritsotakis, M., Voudouris, K., & Anagnostopoulou, C. (2016). Drought  
748 impacts on the fresh water potential of a karst aquifer in Crete, Greece. *Environmental Earth  
749 Sciences*, 75(6). doi: 10.1007/s12665-016-5509-5
- 750 Sweijen, T., Aslannejad, H., & Hassanizadeh, S. M. (2017). Capillary pressure–saturation relationships  
751 for porous granular materials: Pore morphology method vs. pore unit assembly method.  
752 *Advances in Water Resources*, 107, 22–31. doi: 10.1016/j.advwatres.2017.06.00
- 753 Takahashi, M., Momii, K., & Luyun, R. (2018). Laboratory Scale Investigation of Dispersion Effects on  
754 Saltwater Movement due to Cutoff Wall Installation. *E3S Web of Conferences*, 54, 00038. doi:  
755 10.1051/e3sconf/20185400038
- 756 Vithanage, M., Engesgaard, P., Jensen, K., Illangasekare, T., & Obeysekera, J. (2012). Laboratory  
757 investigations of the effects of geologic heterogeneity on groundwater salinization and flush-  
758 out times from a tsunami-like event. *Journal of Contaminant Hydrology*, 136-137, 10–24. doi:  
759 10.1016/j.jconhyd.2012.05.001Van Genuchten, M.T., 1980. A closed-form equation for  
760 predicting the hydraulic conductivity
- 761 Voss, C., Provost, A., 2010. SUTRA—a Model for Saturated–unsaturated, Variable-density Ground-  
762 water Flow with Solute or Energy Transport, 2010. US Geological Survey Water-Resources  
763 Investigations Report, 02-4231.
- 764 Voss, C. I., & Souza, W. R. (1987). Variable density flow and solute transport simulation of regional  
765 aquifers containing a narrow freshwater-saltwater transition zone. *Water Resources  
766 Research*, 23(10), 1851-1866.
- 767 White, W. B., Culver, D. C., & Pipan, T. (2019). *Encyclopedia of caves*. London: Elsevier, Academic Press.
- 768 Xu, Z., Bassett, S. W., Hu, B., & Dyer, S. B. (2016). Long distance seawater intrusion through a karst  
769 conduit network in the Woodville Karst Plain, Florida. *Scientific Reports*, 6(1). doi:  
770 10.1038/srep32235
- 771 Xu, Z., & Hu, B. X. (2017). Development of a discrete-continuum VDFST-CFP numerical model for  
772 simulating seawater intrusion to a coastal karst aquifer with a conduit system. *Water  
773 Resources Research*, 53(1), 688–711. doi: 10.1002/2016wr018758

774 Xu, Z., Hu, B. X., & Ye, M. (2018). Numerical modeling and sensitivity analysis of seawater intrusion in  
775 a dual-permeability coastal karst aquifer with conduit networks. *Hydrology and Earth System*  
776 *Sciences*, 22(1), 221–239. doi: 10.5194/hess-22-221-2018

777 Xu, Z., Hu, B. X., Xu, Z., & Wu, X. (2019). Simulating seawater intrusion in a complex coastal karst  
778 aquifer using an improved variable-density flow and solute transport–conduit flow process  
779 model. *Hydrogeology Journal*, 27(4), 1277–1289. doi: 10.1007/s10040-018-1903-2

780 Zhao, J., Lin, J., Wu, J., Yang, Y., & Wu, J. (2016). Numerical modeling of seawater intrusion in  
781 Zhoushuizi district of Dalian City in northern China. *Environmental Earth Sciences*, 75(9). doi:  
782 10.1007/s12665-016-5606-5

783

784

785

786

787

788

789

790

791

792

793

794

795

796

797

798

799

800

801

802

803

804

805 **Tables**

806 Table 1: Summary of the discrete fracture model parameters

Input parameters	Values
Domain length (m)	0.38
Domain height (m)	0.134
Element size (m)	$1.22 \times 10^{-3}$
Freshwater density ( $\text{kg/m}^3$ )	1000
Saltwater density ( $\text{kg/m}^3$ )	1025
Freshwater head (m)	0.134
Saltwater head (m)	0.128 -0.13
Porous medium (matrix)	
Permeability ( $\text{m}^2$ )	$1.83 \times 10^{-9}$
Porosity	0.385
Fracture	
Permeability ( $\text{m}^2$ )	$1.83 \times 10^{-7}$
Porosity	1
Longitudinal dispersivity (m)	$10^{-3}$
Transverse dispersivity (m)	$3.75 \times 10^{-5}$
Van Genuchten parameters	
$\alpha$ (1/Pa)	$8.45 \times 10^{-4}$
n	4.5
Time step (sec)	1
Simulation time (min)	
Simulating exp. aquifers	50-70
Sensitivity Analysis	80

807

808 Table 2: Steady-state toe length values of the seven investigated laboratory aquifers, and the  
809 corresponding relative change in TL generated during the experimental intrusion ( $dH = 6 - 4$  mm) and  
810 retreat ( $dH = 4 - 5$  mm) phases

Aquifer TL (cm)	dH = 6 mm	dH = 4 mm	dH = 5 mm	$\Delta TL\%_{6-4\text{mm}}$	$\Delta TL\%_{4-5\text{mm}}$
homogeneous	12.10	25.38	14.29	+109.75	-43.70
horizontal-long	2.94	28.89	17.06	+882.65	-40.95
horizontal-middle	8.22	30.14	14.82	+266.67	-50.83
horizontal-left	6.57	20.34	10.87	+209.59	-46.56
horizontal-right	14.94	23.64	17.86	+58.23	-24.45
vertical-middle	9.44	23.91	14.82	+153.28	-38.02
vertical-right	10.30	25.25	15.06	+145.15	-40.36

811

812 Table 3: Comparison between the experimental values of toe length, width of the mixing zone and  
813 percentage of saline volume of the six investigated fractured aquifers and the ones of the equivalent  
814 homogeneous aquifer

Fractured aquifer	Fractured / Homogeneous (%)		
	TL	WMZ	Saline Volume
horizontal-long	113.82	220.74	49.11
horizontal-middle	118.76	285.01	105.98
horizontal-left	80.15	120.92	78.27
horizontal-right	93.12	151.93	93.47
vertical-middle	97.22	150.66	97.89
vertical-right	99.51	244.95	100.88

815

816

817

818

819

820

821

822

823

824

825

826

827

828

829

830

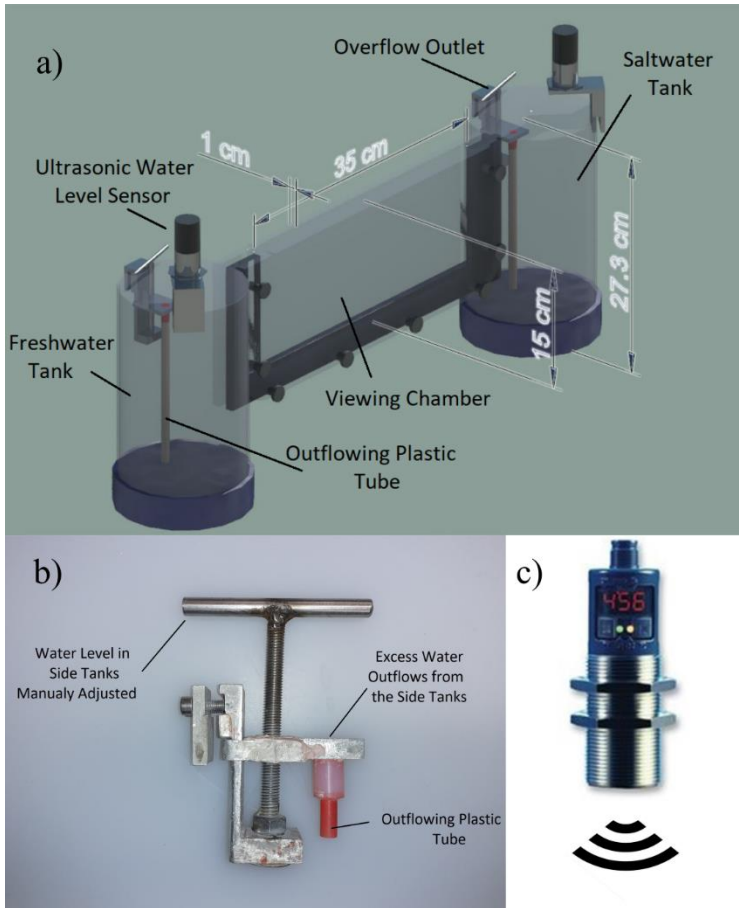
831

832

833

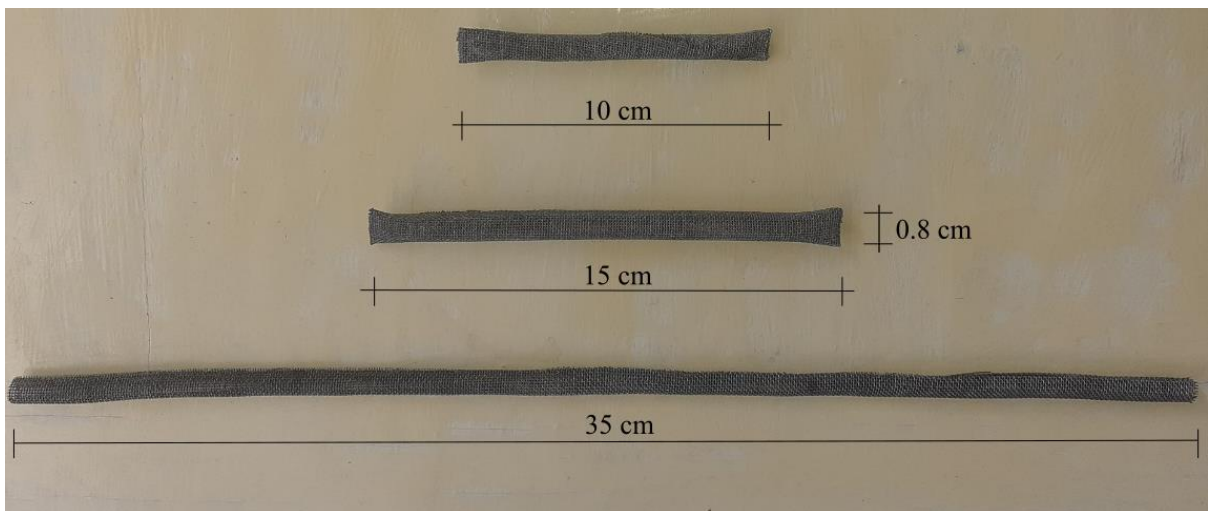
834

835 **Figures**



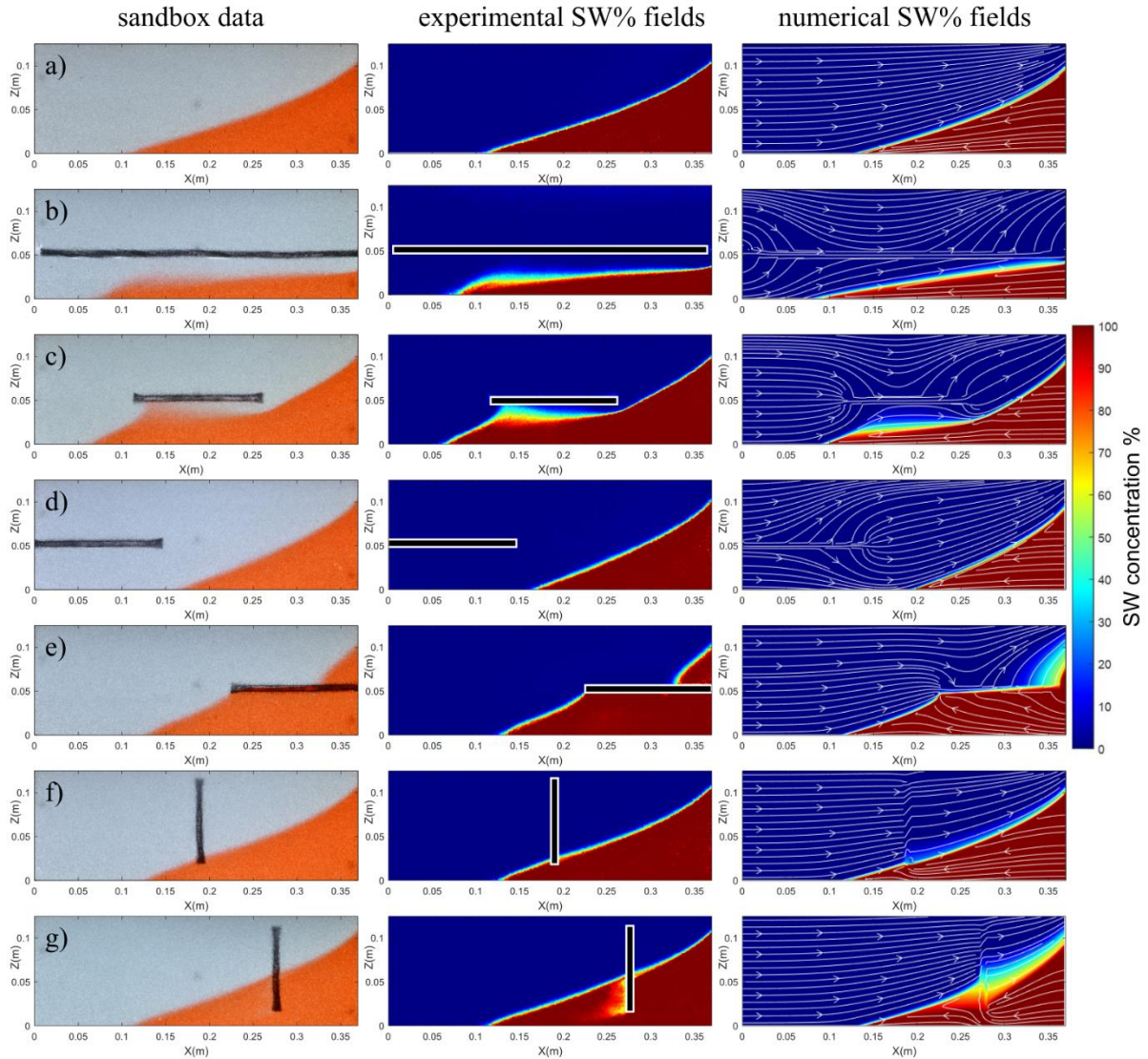
836

837 Figure 1: a) 3-dimensional representation of the utilized experimental setup alongside photos of the  
 838 b) adjustable overflow outlets and c) ultrasonic sensors



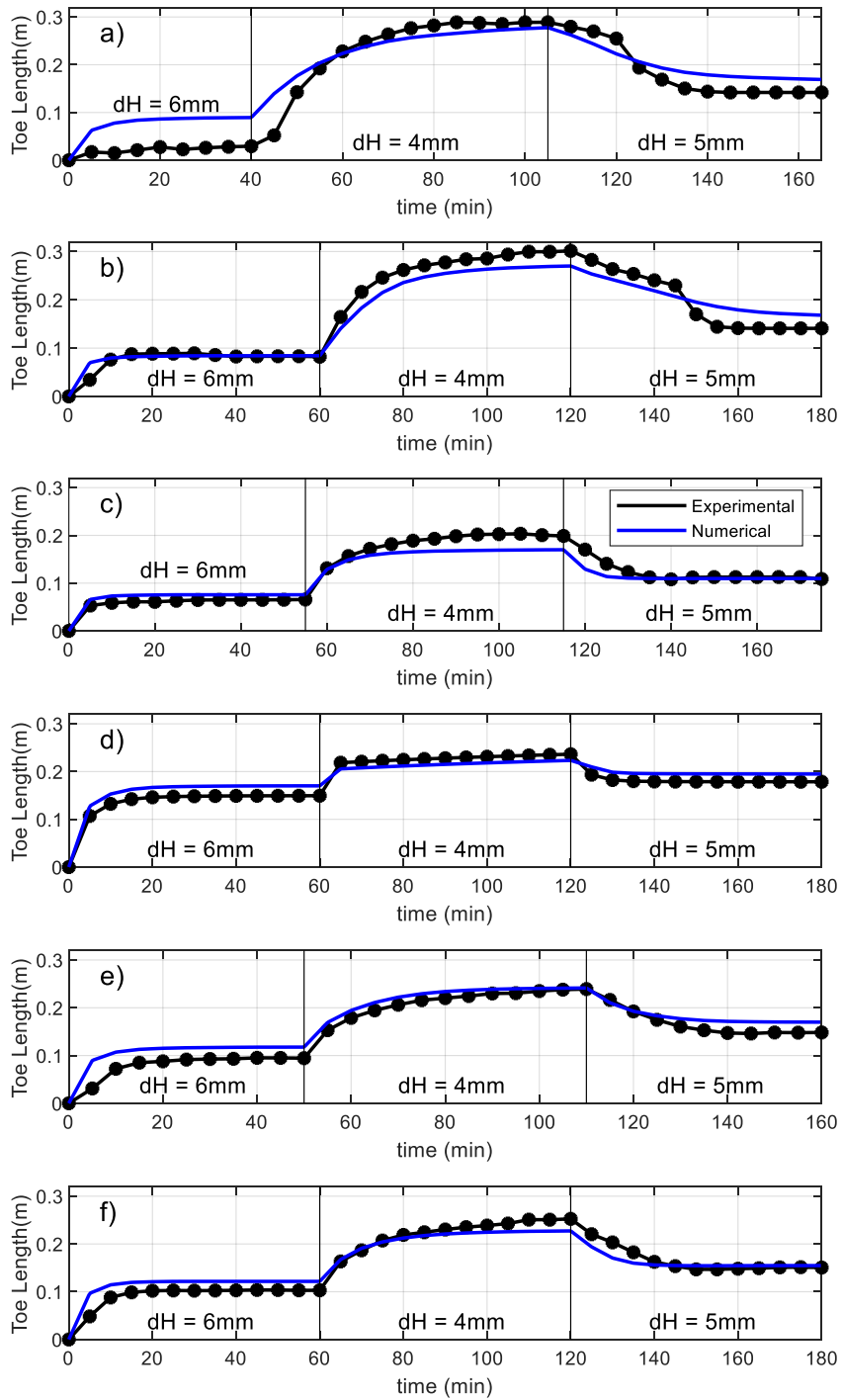
839

840 Figure 2: The three hollow mesh cylinders employed to recreate the aquifer fractures during  
 841 experimental measurements



842

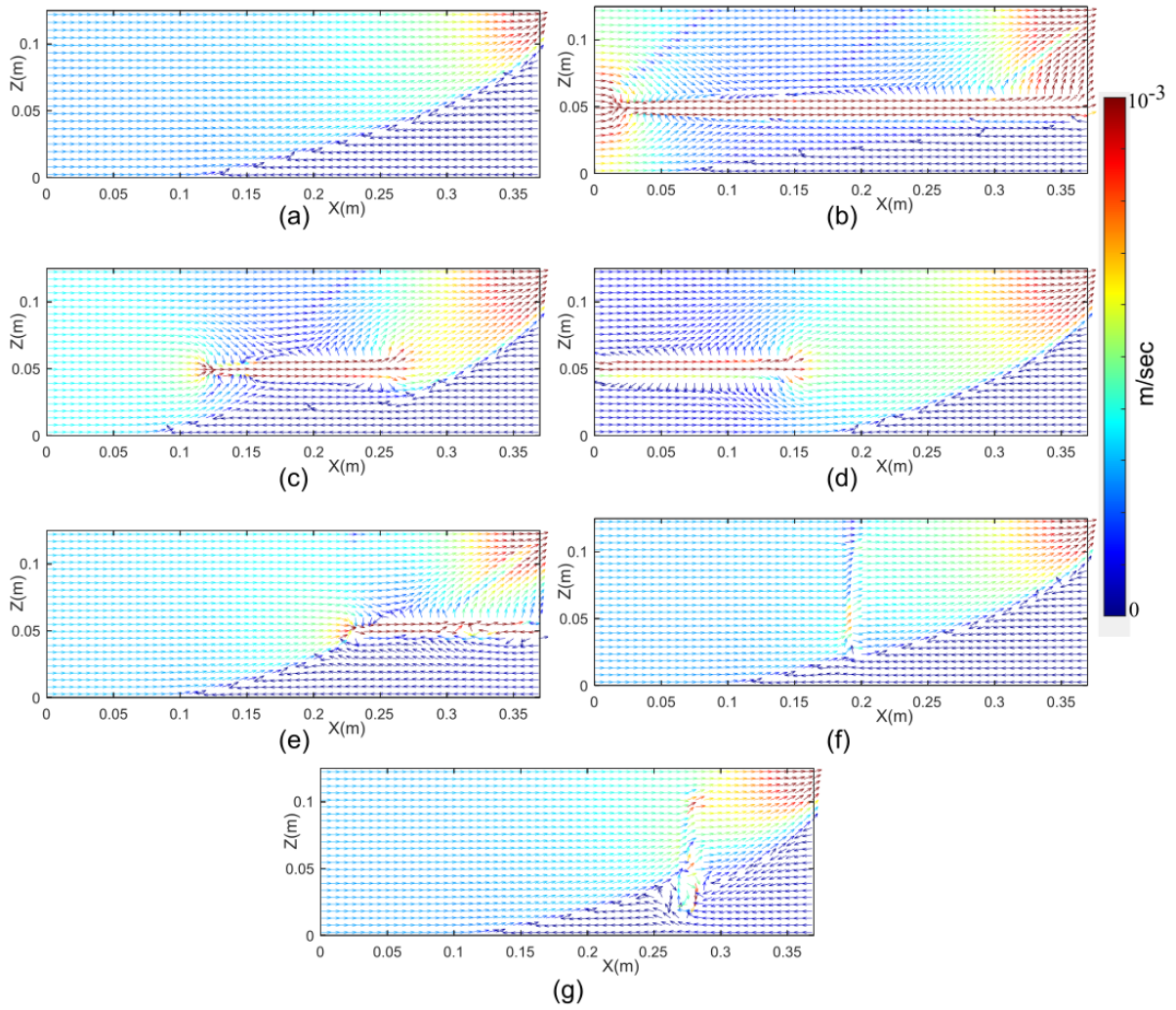
843 Figure 3: Photos of laboratory induced saline intrusion alongside experimental and numerical  
 844 saltwater concentration fields in the seven investigated aquifers. From top to bottom the investigated  
 845 cases are a) homogeneous aquifer, b) horizontal-long, c) horizontal-middle, d) horizontal-left, e)  
 846 horizontal-right, f) vertical-middle and g) vertical-right fractured aquifers.



847

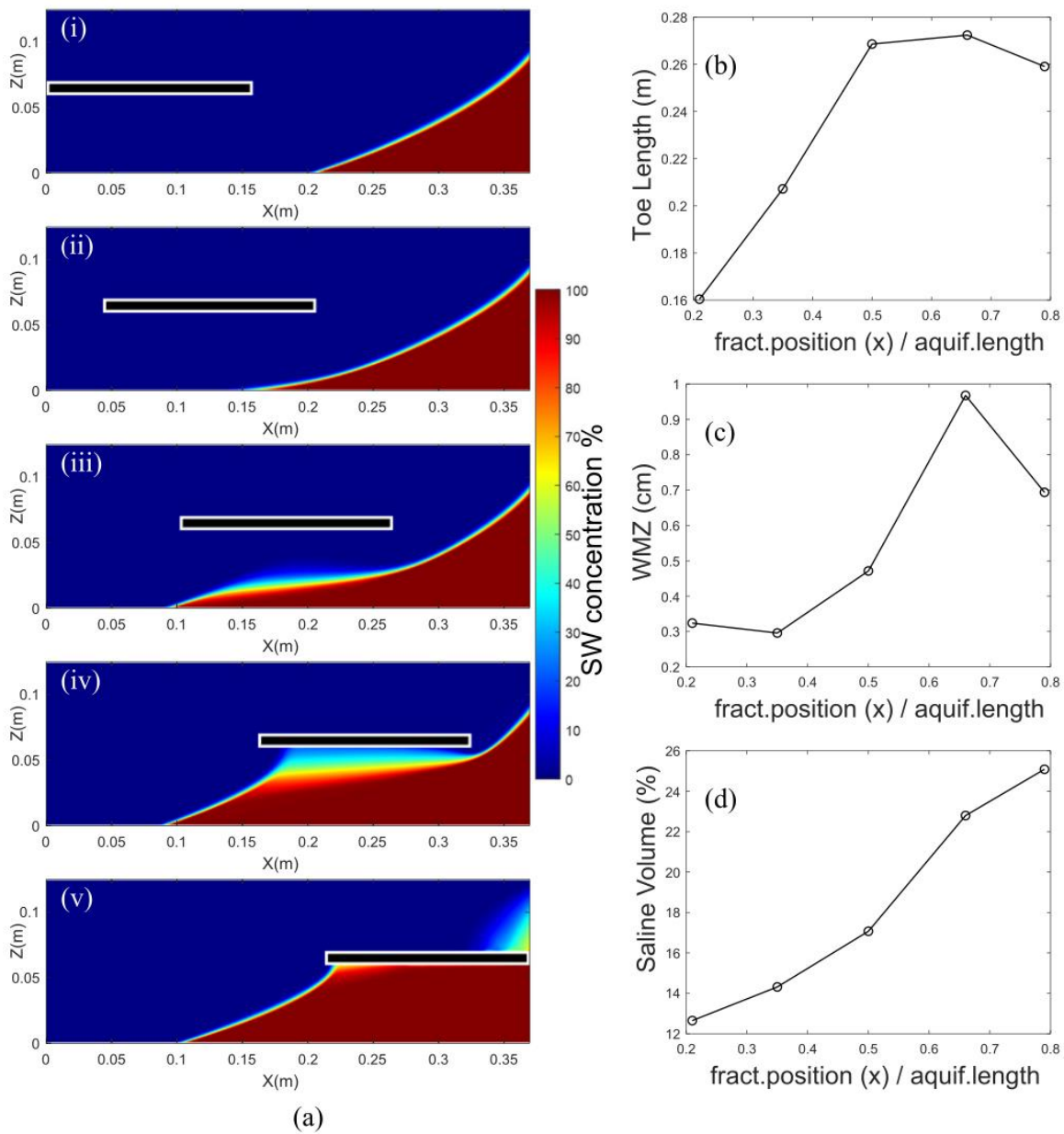
848 Figure 4: Experimental and numerical transient toe length values of the a) horizontal-long, b)  
 849 horizontal-middle, c) horizontal-left, d) horizontal-right, e) vertical-middle and f) vertical-right  
 850 fractured aquifers





851

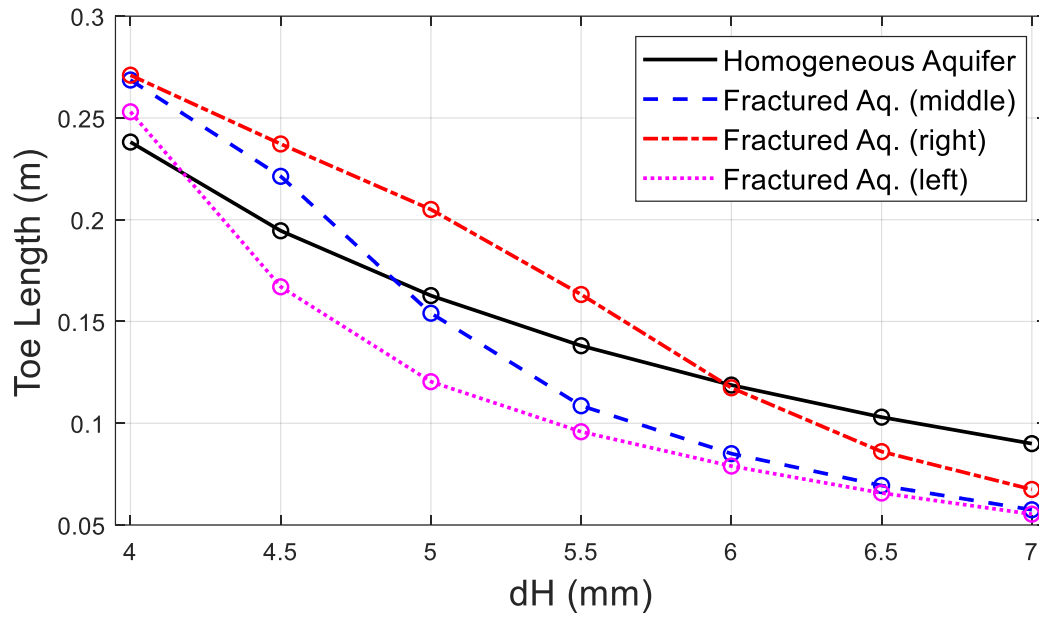
852 Figure 5: Flow velocity vector fields, generated by a hydraulic head difference of 4 mm for the a)  
 853 horizontal-long, b) horizontal-middle, c) horizontal-left, d) horizontal-right, e) vertical-middle, f)  
 854 vertical-right fractured and the g) homogeneous aquifer



855

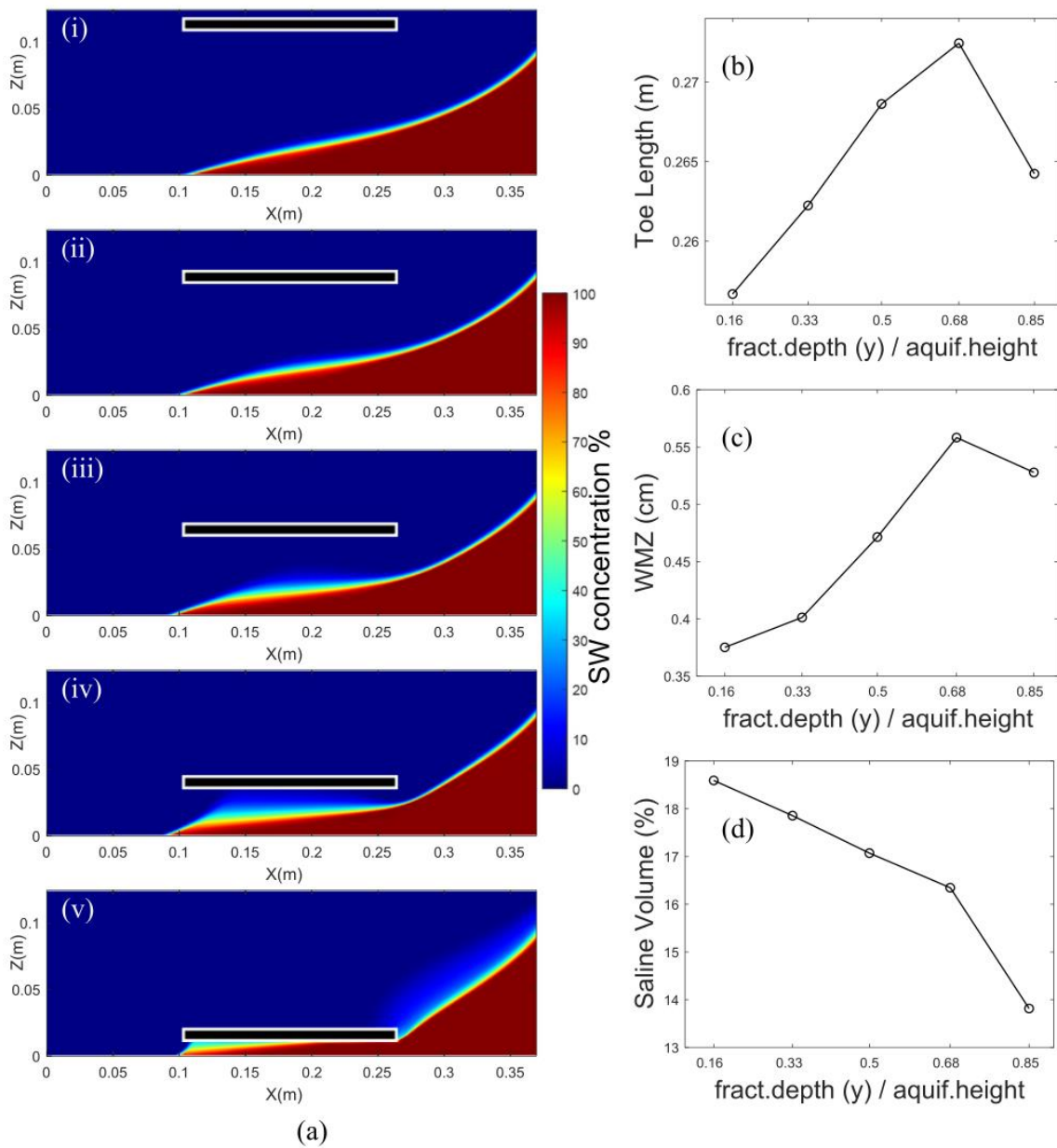
856 Figure 6: Simulated a) SW concentration fields alongside their corresponding values of b) toe length,  
 857 c) width of mixing zone and d) percentage of saline volume, demonstrating the impact of position (x)  
 858 of a horizontal fracture on aquifer SWI

859



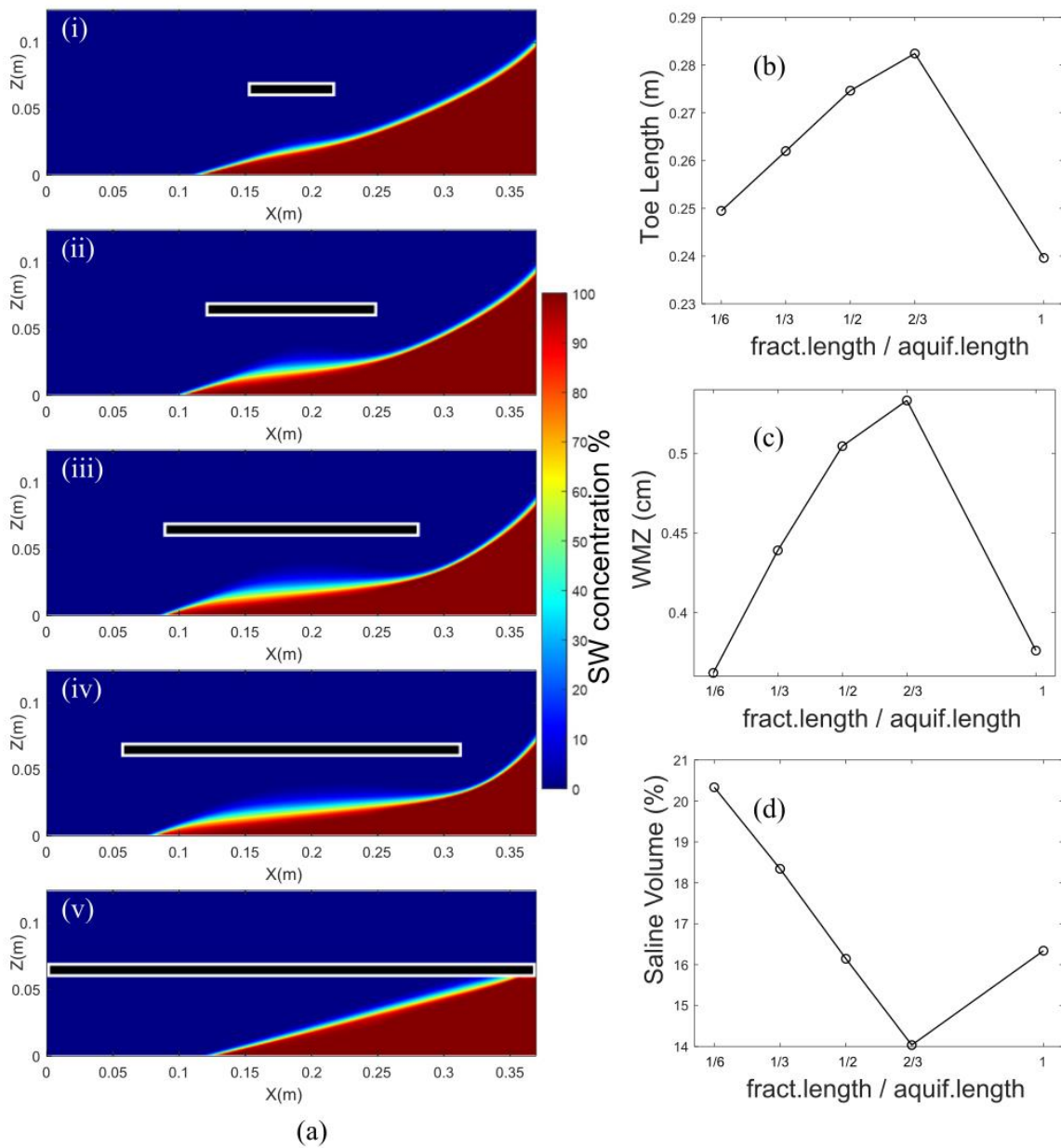
860

861 Figure 7: Values of saltwater toe length generated by the application of seven distinct hydraulic head  
 862 difference values ( $dH = 4 \text{ mm} - 7 \text{ mm}$ ) in one homogeneous (black) and three heterogeneous aquifers,  
 863 containing a single horizontal fracture at their right (red) and left (purple) side, and their middle (blue)  
 864 respectively



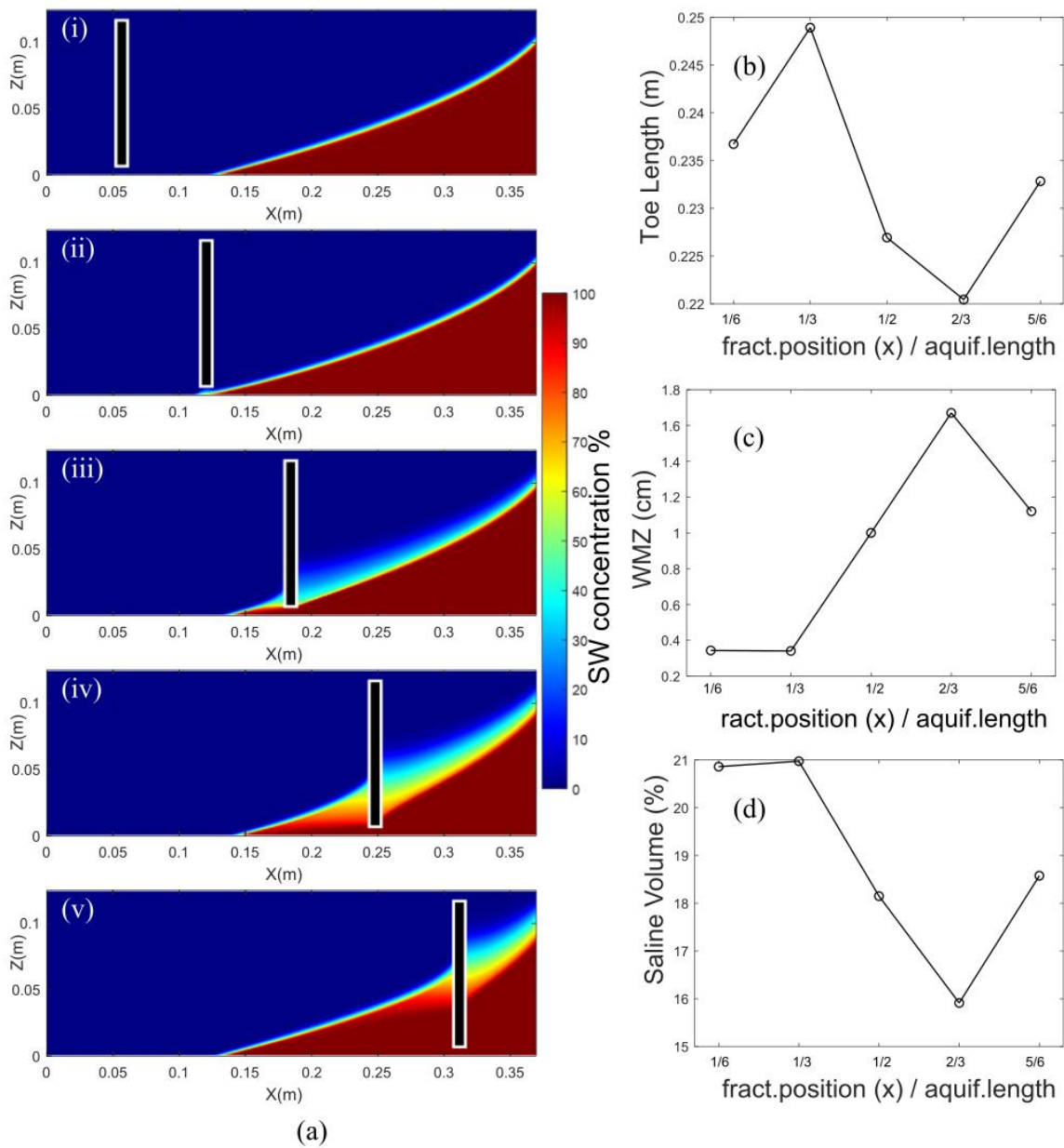
865

866 Figure 8: Simulated a) SW concentration fields alongside their corresponding values of b) toe length,  
 867 c) width of mixing zone and d) percentage of saline volume, demonstrating the impact of position (z)  
 868 of a horizontal fracture on aquifer SWI



869

870 Figure 9: Simulated a) SW concentration fields alongside their corresponding values of b) toe length,  
 871 c) width of mixing zone and d) percentage of saline volume, demonstrating the impact of a horizontal  
 872 fracture's length on aquifer SWI



873

874 Figure 10: Simulated a) SW concentration fields alongside their corresponding values of b) toe length,  
 875 c) width of mixing zone and d) percentage of saline volume, demonstrating the impact of position (x)  
 876 of a vertical fracture on aquifer SWI

877

878

879

880

881